

# LLE Review

## Quarterly Report



April–June 1988

Laboratory for Laser Energetics  
College of Engineering and Applied Science  
University of Rochester  
250 East River Road  
Rochester, New York 14623-1299



# LLE Review

## Quarterly Report

*Editor:* R. Kremens  
(716) 275-4548

April–June 1988

---

Laboratory for Laser Energetics  
College of Engineering and Applied Science  
University of Rochester  
250 East River Road  
Rochester, New York 14623-1299



This report was prepared as an account of work conducted by the Laboratory for Laser Energetics and sponsored by Empire State Electric Energy Research Corporation, New York State Energy Research and Development Authority, Ontario Hydro, the University of Rochester, the U.S. Department of Energy, and other United States government agencies.

Neither the above named sponsors, nor any of their employees, makes any warranty, expressed or implied, or assumes any legal liability or responsibility for the accuracy, completeness, or usefulness of any information, apparatus, product, or process disclosed, or represents that its use would not infringe privately owned rights.

Reference herein to any specific commercial product, process, or service by trade name, mark, manufacturer, or otherwise, does not necessarily constitute or imply its endorsement, recommendation, or favoring by the United States Government or any agency thereof or any other sponsor.

Results reported in the LLE Review should not be taken as necessarily final results as they represent active research. The views and opinions of authors expressed herein do not necessarily state or reflect those of any of the above sponsoring entities.

## **IN BRIEF**

This volume of the LLE Review, covering the period April–June 1988, contains an in-depth article on recent cryogenic target experiments on the OMEGA laser system; two articles on laser-plasma interactions; and an advanced technology article discussing laser damage in polymeric materials. Finally, the activities of the National Laser Users Facility and the GDL and OMEGA laser facilities are summarized.

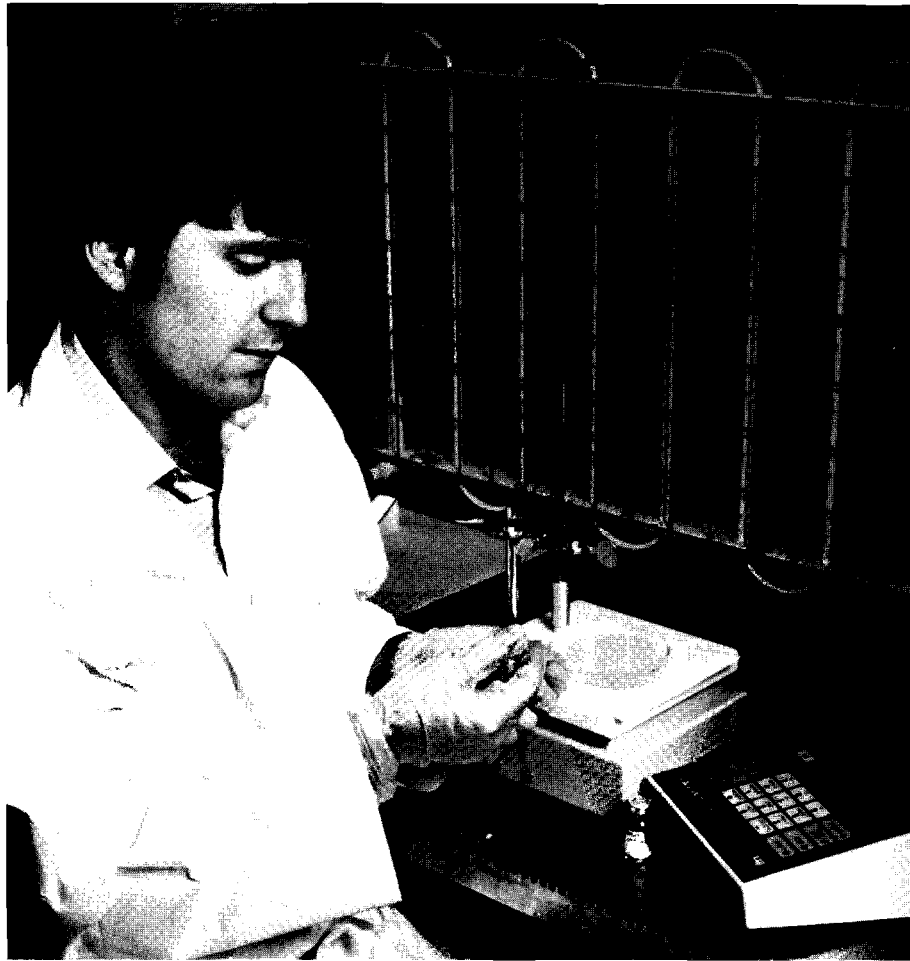
The following are highlights of the research reports contained in this issue:

- Direct-drive laser-fusion experiments have been performed on cryogenically cooled targets. For the first time, compressed fuel density in the range of 100 to 200 times that of liquid DT was measured by direct means, using a knock-on technique developed at LLE.
- Anomalous burn-through of multilayer targets has been investigated. It was shown that initial low-intensity plasma formation effects might have a significant influence on subsequent hydrodynamics of laser-fusion targets.
- Burn-through times have been measured for parylene-coated targets in an attempt to gauge time-resolved illumination uniformity. Evidence of high-intensity hot spots for a small fraction of the beam energy was observed.

- Laser damage in  $\pi$ -electron molecular and polymeric materials has been measured. The OMEGA laser system is one of the first to employ these organic materials in optics in large numbers. These materials may offer “designer” solutions to some optical problems.

# CONTENTS

	<i>Page</i>
IN BRIEF .....	iii
CONTENTS .....	v
Section 1 PROGRESS IN LASER FUSION .....	97
1.A Cryogenic Laser-Fusion Target Experiments .....	97
1.B Effect of Barrier Layers on Burn-Through Time in Parylene .....	113
1.C Barrier-Layer Experiments and Initial Plasma Formation in Laser Plasma .....	125
Section 2 ADVANCED TECHNOLOGY DEVELOPMENTS .....	130
2.A Laser Damage in $\pi$ -Electron Systems .....	130
Section 3 NATIONAL LASER USERS FACILITY NEWS .....	137
Section 4 LASER SYSTEM REPORT .....	138
4.A GDL Facility Report .....	138
4.B OMEGA Facility Report .....	139
PUBLICATIONS AND CONFERENCE PRESENTATIONS	



Kevin Skerrett, a laboratory engineer in the Optical Materials Group, is shown filling a liquid-crystal circular polarizer. The device is used to maintain circular polarization through the amplification stages of OMEGA.

# Section 1

## PROGRESS IN LASER FUSION

### 1.A Cryogenic Laser-Fusion Target Experiments

Direct-drive laser fusion is accomplished by uniformly illuminating spherical fuel-bearing pellets with high-power laser beams, causing their implosion and subsequent manyfold increase in density and temperature. Recently, short-wavelength lasers have been found to be capable of efficient compression of fusion pellets due to the creation of large ablation pressures ( $\geq 20$  Mbar) while producing few suprathreshold electrons, which tend to preheat the fuel and degrade the compression.<sup>1,2</sup> Eventually, for inertial confinement fusion (ICF) to become an economical method for producing power, a gain in energy in excess of 100 must be produced from a fusion pellet. It has been estimated that the DT fuel in such a pellet must be compressed to  $\sim 1000$  times liquid density (XLD) and reach a temperature of 4 to 5 keV in the central region for thermonuclear ignition and efficient burn to occur.<sup>3</sup>

In order to obtain efficient compression of a target, the fuel should initially be at a low temperature and be compressed adiabatically. If enough fuel is compressed in this way and heating of the fuel occurs at the final stages of the implosion, then ignition of the fuel and a net gain of energy will occur. A simple way to achieve high compression of fusion fuel is to cool the target cryogenically so that the fuel is initially a solid levitated against the inside edge of the pusher. In addition to the low initial temperature, the solid state of the fuel makes it impossible for shocks propagating through the fuel layer to reach the origin and rebound, causing fuel preheat. Other requirements needed



to compress fusion fuel on a low adiabat are pulse shaping and low preheating of the fuel.<sup>4</sup>

In this article we describe direct-drive laser-fusion experiments performed on cryogenically cooled targets that were compressed by the short-wavelength (351-nm) beams of the OMEGA laser system. While not all of the necessary requirements for low-adiabat, nearly isentropic compression<sup>4</sup> are met in these experiments, the use of cryogenic targets makes it possible to study the performance of fusion-fuel targets designed to obtain high peak fuel densities. The targets consisted of simple glass microballoons filled with high-pressure DT gas. These targets were held in place on ultra-low-mass supports inside a cryogenically cooled housing positioned inside the OMEGA target chamber. The targets used in these experiments were prepared for an implosion experiment by a technique that optimizes the uniformity of the frozen-fuel layer.

Target performance was extensively characterized by a set of x-ray, plasma, and nuclear instruments. The x-ray and plasma diagnostics, which principally measured laser-target interaction, included the following: plasma calorimeters, charge collectors, an x-ray calorimeter, an x-ray microscope, a streaked x-ray spectrograph, and a time-resolved, soft x-ray diode array. Neutron and particle diagnostics, which were sensitive mainly to the thermonuclear reaction products, included the following: a set of neutron counters, a detector system for measuring the activation of target-shell material by the thermonuclear neutrons, knock-on detectors, and a set of neutron time-of-flight detectors. Typical target performance recorded was of  $\sim 70\%$  absorption, maximum shell velocities of  $\sim 3 \times 10^7$  cm s<sup>-1</sup>, neutron yields of  $10^6$  to  $10^8$ , and final fuel areal densities of 20 to 40 mg cm<sup>-2</sup>. Fuel densities at the time of thermonuclear neutron production, estimated from measurements of fuel areal density ( $\rho R$ ), were in the range of 100 to 200 times the density of liquid DT for the optimum targets examined in these experiments.

Previous experiments<sup>5</sup> have reported fuel densities in the range of 100 XLD using nuclear activation techniques that measure the shell areal density ( $\rho \Delta R$ ) of the material surrounding the compressed fuel. The compressed-fuel densities were inferred from the measured  $\rho \Delta R$  using the assumptions of mass conservation, a one-dimensional model of the compressed core, and pressure balance between shell and fuel. The measurements of  $\rho R$  and inferred values of fuel density presented in this work are not dependent on assumed or actual values of shell areal density, temperature of the imploded material, or amount of fuel-shell mixing; they are the first such measurements of highly compressed thermonuclear fuel.

## Experiments

### 1. Laser Conditions

Recent modifications of the OMEGA system that were used in these experiments include liquid-crystal polarizers,<sup>6</sup> which enabled circularly polarized radiation to be propagated through the entire front end of the amplifier system, thereby minimizing stress birefringence induced by

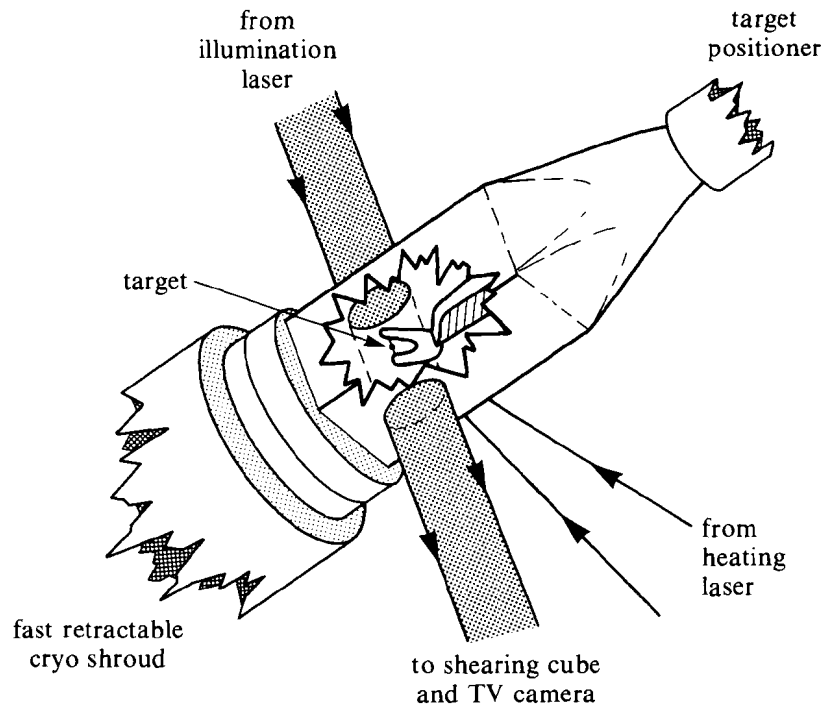
the rod amplifiers, and distributed phase plates, to increase the uniformity of the target irradiation.<sup>7</sup>

Typical performance of the OMEGA system during these experiments was with output energy of 125 J per beam at 1054 nm in a 750-ps pulse (FWHM), with a corresponding frequency-tripled output per beam of 75 J in a 650-ps pulse. Beam diameters were 17 cm (95% intensity) at the output of the frequency-tripling crystals. Individual beam energies were measured by reflection of a small fraction of the beam into integrating calorimeters that measured the  $1\omega$ ,  $2\omega$ , and  $3\omega$  components of the conversion-crystal output with a beam-to-beam accuracy of 1% and an absolute accuracy of 1%–2%. The beam-on-target arrival time was adjusted to be coincident to within 3 ps. The per-beam energy on target was estimated by measuring the loss in energy incurred as the beam traveled from the output of the conversion crystals into the target chamber. As so estimated, the variation in beam-to-beam energy was reduced to an average of  $\sim 5\%$  ( $\sigma_{\text{rms}}$ ) for these experiments. The 24 beams of OMEGA were focused onto the target by  $f/3.7$ , 566-mm-focal-length, AR-coated-fused-silica, aspherical single-element lenses. Individual beam pointing was verified to an accuracy of  $\sim 10\ \mu\text{m}$  or less of lateral displacement from the target center and  $\sim 50\ \mu\text{m}$  or less of transverse displacement from the target center.

The on-target illumination uniformity was enhanced for these experiments by incorporating a distributed phase plate (DPP)<sup>7</sup> into each beam at the position of the final focus lens. The DPP's modify the phase front of the OMEGA beams (phase-front errors have been found to be the dominant source of intensity nonuniformities at the target plane<sup>8</sup>) by shifting the phase of the beam by a randomly assigned amount of either 0 or  $\pi$  in approximately 10,000 hexagonally shaped subregions of the beam. Each phase plate therefore produces the equivalent of 10,000 beamlets; the combined effect of the phase plates used in the 24 OMEGA beams is to irradiate the target with  $\sim 240,000$  beamlets. The DPP's provide an improved target irradiation uniformity with a slight reduction ( $\sim 20\%$ ) in the average intensity. The variation in illumination uniformity due to DPP-modified OMEGA beams has been estimated to be  $\sim 8\%$  ( $\sigma_{\text{rms}}$ ) if thermal smoothing in the plasma by 1% of the beam diameter ( $\sim 3\ \mu\text{m}$ ) is assumed to occur.<sup>7</sup> In actual experiments a larger variation in intensity uniformity occurs, due principally to the beam-to-beam energy output variation [which was  $< 9\%$  ( $\sigma_{\text{rms}}$ ) for all experiments]. The combined variation in intensity uniformity is therefore estimated to have been  $\leq 12\%$  ( $\sigma_{\text{rms}}$ ) for these experiments.

## 2. Targets

Implosion experiments were performed on simple glass microballoons containing DT at pressures of 75 to 100 atm. The targets were nominally filled with an equimolar mixture of deuterium and tritium. The targets were mounted, using no glue, on a support structure that was compatible with the cryogenic target-positioning system (Fig. 35.1).<sup>9</sup> The targets were supported by spider silks drawn across a *U*-shaped copper mount whose width (3 mm) and thickness



E4481

Fig. 35.1

Schematic of the target assembly as it would appear positioned inside the cooling shroud. The heating laser and interferometer system are used to optimize the thickness uniformity of the solid DT layer.

(100  $\mu\text{m}$ ) were constrained by the requirement that the horseshoe be narrow enough to fit in the liquid-He-cooled target shroud and thin enough not to obscure the converging OMEGA beams. A target was assembled onto its mount by placing it on a cradle consisting of two spider silks drawn across a *U* mount, after which additional spider silks (one to three) were placed over and under the target to hold it in place. Next, the target-mount assembly was coated with a 0.2- $\mu\text{m}$  flash of parylene to give it additional mechanical stability.

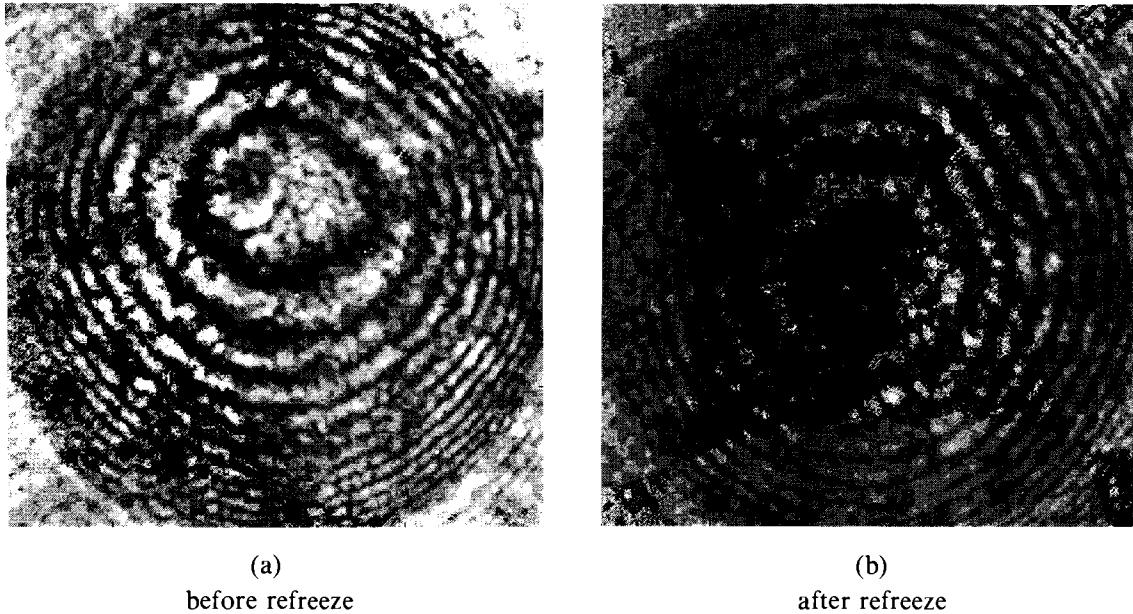
### 3. Cryogenic Target System

Targets mounted as described above were positioned and cooled to below the freezing point of DT (19°K) by the OMEGA cryogenic target-positioning system (cryo system), which is described in detail in Ref. 11. The system consists of four subsystems: (1) a liquid He-cooled target positioner; (2) a fast, retractable, liquid-He-cooled shroud; (3) a heating laser system used to vaporize rapidly the frozen fuel while the target is inside the cooled shroud; and (4) a shearing interferometer system used to document the thickness and uniformity of the frozen fuel layer.

Preparation of the cryogenic target is based on the fast-refreeze technique developed by KMS Fusion.<sup>10</sup> Targets were prepared for implosion experiments as follows: The target was placed in the OMEGA chamber and cooled to below the DT freezing point in a

liquid-He-cooled shroud. The uniformity of the frozen-fuel layer was then optimized by repeatedly heating this layer with an Ar-ion laser, followed by rapid cooling, until a layer with good uniformity was obtained. [Figures 35.2(a) and 35.2(b) show interferograms of a cryo target before and after preparation by the fast-refreeze technique.] Estimates of the uniformity of the fuel layer obtainable with this technique were made by ray-tracing simulation. These simulations indicated that symmetry of the interferogram to within 0.5 fringes implied a fuel-layer uniformity with a  $\leq 20\%$  variation in layer thickness. (This variation was the limit to which variations could be detected interactively and representative of the uniformity of the initial fuel layer in the implosion experiments.) Finally,  $\sim 40$  ms before target irradiation, the cooling shroud was rapidly extracted, exposing the target to the ambient environment for  $\sim 10$  ms. (The length of time required for the DT to melt was  $\sim 30$  ms.)

Interferograms of 300- $\mu\text{m}$ -diameter GMB with 5- $\mu\text{m}$  DT layer



E4482

Fig. 35.2

Interferograms of a 300- $\mu\text{m}$ -diameter glass microballoon (a) before and (b) after preparation by the fast-refreeze technique. The prepared target (b) has a nearly uniform solid DT layer with a thickness of 5  $\mu\text{m}$ .

### Target Design

Target design and prediction of target performance was accomplished with the one-dimensional (*LILAC*) and two-dimensional (*ORCHID*) hydrodynamic simulation codes. Both codes use tabular equation of state (*SESAME*),<sup>11</sup> flux-limited electron thermal transport, multifrequency group radiation transport with local thermodynamic equilibrium (*LTE*) opacities,<sup>12</sup> and inverse-bremsstrahlung-absorption energy deposition through a ray-tracing algorithm in the underdense plasma.

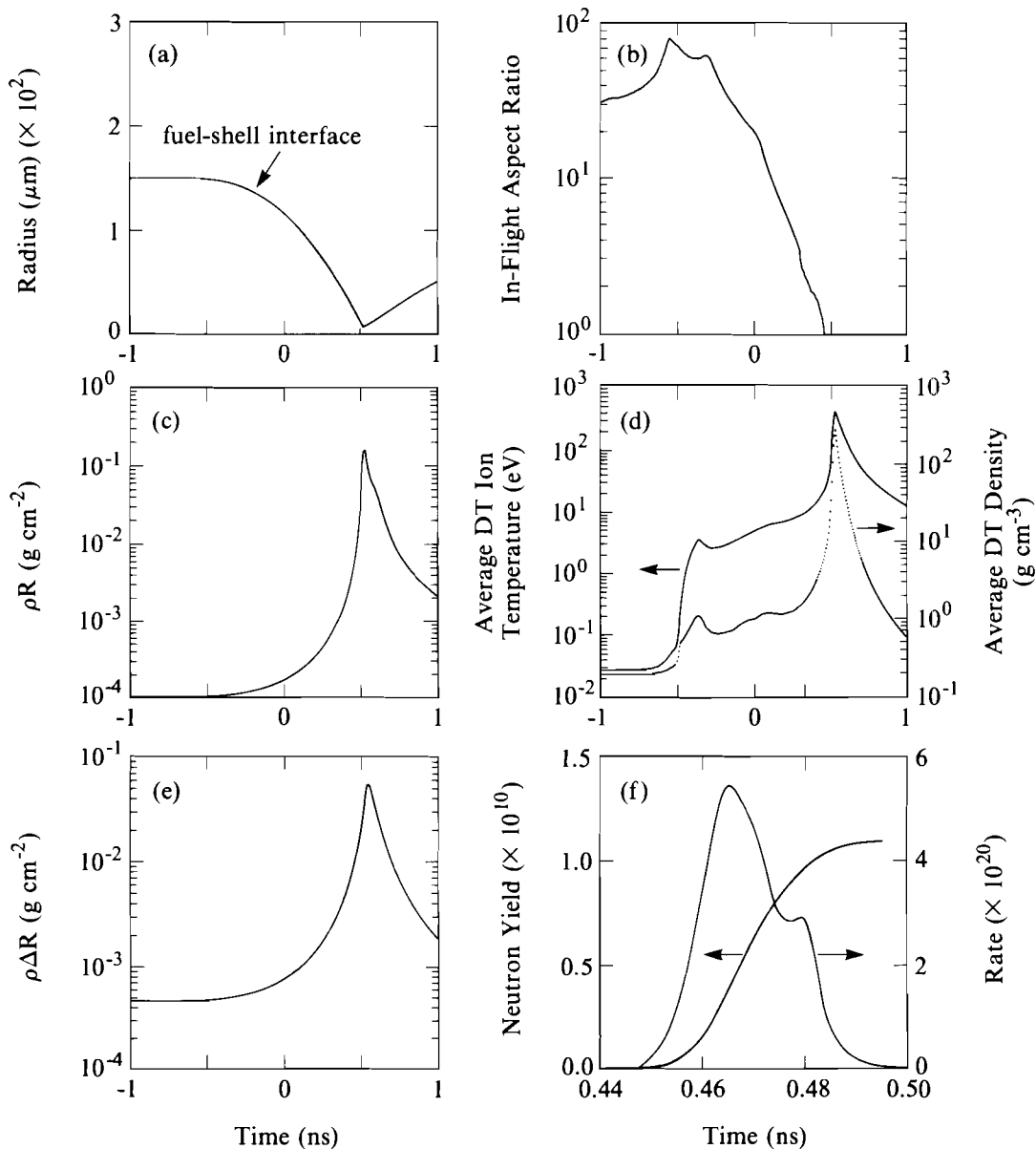
Figures 35.3(a)-35.3(f) show the *LILAC*-calculated target behavior for a typical cryo experiment. In this example, the target is a 150- $\mu\text{m}$  inner radius ( $R_0$ ) glass microballoon having a 5- $\mu\text{m}$  wall ( $\Delta R_0$ ) and containing 100 atm of DT frozen into a 5- $\mu\text{m}$  layer of ice. The target is assumed to be irradiated with 1200 J of UV radiation in a 650-ps (FWHM) Gaussian pulse, which was the typical illumination condition for these experiments. Figures 35.3(a) and 35.3(b) show the fuel-shell interface trajectory and the time history of the in-flight aspect ratio ( $R/\Delta R$ ), respectively. Initially, the shell is compressed, reaching an aspect ratio of  $\sim 70$  at  $\sim 500$  ps before the peak of the pulse, followed by a continuous decompression of the shell, due to radiative heating, as the implosion progresses. The fuel and shell begin to accelerate rapidly at  $\sim 400$  ps before the peak of the pulse. The fuel density  $\rho$  rises to a peak value of  $\sim 300$  g  $\text{cm}^{-3}$  and reaches an average temperature of 0.5 keV during the stagnation phase [Fig. 35.3(d)]. Peak fuel and shell areal densities [Figs. 35.3(c) and 35.3(e)],  $\rho R$  and  $\rho \Delta R$ , are  $\sim 150$  and  $\sim 50$  mg  $\text{cm}^{-2}$ , respectively. A neutron yield of  $1.1 \times 10^{10}$  is obtained within a 40-ps time interval, coinciding with the time of fuel coalescence at the origin and peak compression [Fig. 35.3(f)]. The average fuel density during the time of neutron production,  $\langle \rho \rangle_n$ , is 210 g  $\text{cm}^{-3}$ , which is lower than the peak density of 300 g  $\text{cm}^{-3}$ . The other neutron-averaged quantities are

$$\begin{aligned} \langle T_i \rangle_n &= 1.2 \text{ keV}, \\ \langle \rho R \rangle_n &= 140 \text{ mg cm}^{-2}, \\ \text{and } \langle \rho \Delta R \rangle_n &= 36.0 \text{ mg cm}^{-2}. \end{aligned}$$

## Results

Cryogenic target experiments were performed on a large number ( $\sim 100$ ) of DT-filled glass microballoons. Optimum conditions for target performance and measurements were determined iteratively by performing implosion experiments and improving target experiment and/or measurement techniques, followed by repeated implosion experiments. Some target experiments were unsuccessful because of unrepeatability circumstances, such as laser-system misfires or target mispositioning during cryo-shroud retraction. Successful, well-diagnosed target experiments were performed principally on glass microballoons filled with 100 atm of DT, having radii of 100 to 150  $\mu\text{m}$  and shell thicknesses of 3 to 7  $\mu\text{m}$ . We have tabulated results of target experiments in Table 35.I for which a complete set of measurements was obtained. The columns of Table 35.I are (1) the OMEGA shot number; (2) the microballoon shell inner radius  $R_0$  ( $\mu\text{m}$ ); (3) the shell thickness  $\Delta R_0$  ( $\mu\text{m}$ ); (4) the incident energy  $E_{\text{inc}}$  (J); (5a) the measured and (5b) the predicted absorbed energy  $E_{\text{abs}}$  (J); (6) the beam balance  $\sigma_{\text{rms}}$  (%); (7a) the measured and (7b) the predicted thermonuclear neutron yield  $Y_N$ ; (8a) the measured and (8b) the predicted neutron-averaged fuel areal density  $\langle \rho R \rangle_n$  (mg  $\text{cm}^{-2}$ ); and (9a) the inferred and (9b) the predicted neutron-averaged fuel density  $\langle \rho \rangle_n$  (g  $\text{cm}^{-3}$ ).

As can be seen by comparing columns 5a and 5b of Table 35.I, the measured and predicted fractions of incident energy absorbed by the



E4631

Fig. 35.3 One-dimensional hydrocode simulations (*LILAC*) of the implosion of a 300-μm-diameter, 5-μm-wall glass microballoon having a 100-atm-DT fill that has been cryogenically cooled, forming a 5-μm solid DT layer. (a) The fuel-shell interface trajectory. (b) The in-flight aspect ratio. (c) The fuel areal density. (d) The fuel temperature and density. (e) The shell areal density. (f) The integrated yield and rate of generation of neutrons during the time of peak compression.

Table 35.I  
Cryogenic Experiment Results

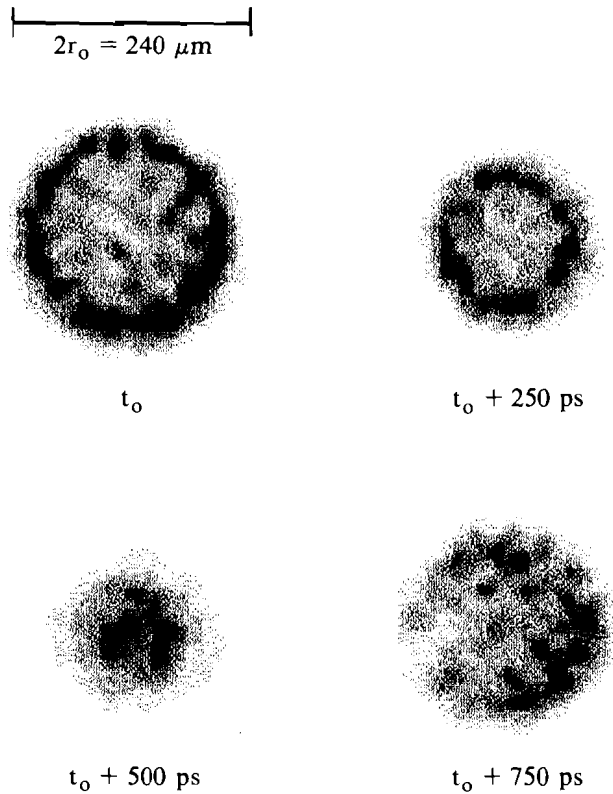
(1) Shot	(2) $R_o$ ( $\mu\text{m}$ )	(3) $\Delta R_o$ ( $\mu\text{m}$ )	(4) $E_{inc}$ (J)	(5) $E_{abs}$ (J)		(6) $\sigma_{rms}$ (%)	(7) $Y_N$ ( $n_e$ 's)		(8) $\langle \rho R \rangle_n$ ( $\text{mg cm}^{-2}$ )		(9) $\langle \rho \rangle_n$ ( $\text{g cm}^{-3}$ )	
				expt	LILAC		expt	LILAC	expt	LILAC	expt	LILAC
16011	192	2.8	—	1186	1176	4.1	8.3 (7)	5.9 (10)	4.4	43.4	0.8	23.8
16054	120	4.9	1080	747	780	4.9	9.2 (6)	1.4 (10)	32.0	96.2	30.0	158.0
16105	110	6.1	1066	768	828	8.7	4.7 (6)	6.2 (9)	35.5	68.1	40.4	107.0
16188	133	3.9	1065	793	764	5.2	1.4 (7)	2.9 (10)	16.6	135.0	11.3	261.0
16212	134	5.0	1138	858	875	7.4	6.4 (6)	1.2 (10)	27.8	130.0	20.9	216.0
16265	111	5.8	951	751	698	8.5	4.7 (6)	6.5 (9)	23.1	64.6	21.1	98.7
16266	137	5.7	1145	926	935	6.9	8.4 (6)	1.7 (10)	26.2	97.0	18.5	132.0
16267	134	5.8	1150	862	927	5.1	8.5 (6)	1.6 (10)	32.5	90.0	26.4	122.0
16268	134	5.7	1207	891	955	3.7	7.6 (6)	1.9 (10)	23.2	94.4	16.0	131.0
16270	103	5.2	1015	658	622	3.8	5.3 (6)	6.1 (9)	20.8	69.4	20.2	123.0
16272	118	7.0	1146	794	878	3.7	4.6 (6)	5.4 (9)	9.6	66.1	5.1	92.5
16279	128	5.9	1137	941	896	3.9	1.1 (7)	1.4 (10)	13.8	81.7	7.8	113.0

E4654

target are in close agreement. Independent measurements of the absorption, the x-ray conversion efficiency, and the mass-ablation rate versus intensity by glass targets irradiated by UV (351-nm) radiation<sup>13</sup> indicate that the partition of laser energy into these forms is well modeled by the one-dimensional code.

#### 1. Time- and Space-Resolved X-Ray Measurements

The x-ray diagnostics are primarily sensitive to emission from the laser-heated shell material. Several of these diagnostics yield information about the state of the shell material during the course of the implosion. Figure 35.4 shows a set of images taken by an x-ray framing camera.<sup>14</sup> The framing camera consisted of a pinhole camera assembly with a 10- $\mu\text{m}$  pinhole array illuminating a gated microchannel plate (MCP). Four x-ray images (frames) were obtained by independently gating four regions of the MCP with short ( $\sim 200$ -ps) high-voltage pulses. The sensitive time of each frame was  $\sim 120$  ps (FWHM), and the frames were separated by 250 ps. There is some spatial smearing in these framed images because the target was in motion; nevertheless, a ring of emission is seen, the radius corresponding to the average shell radius during the frame. Figure 35.5 shows the measured and predicted radius of peak x-ray emission, as determined from framed x-ray images for three cryo target experiments where the target wall thicknesses were 3  $\mu\text{m}$ , 5  $\mu\text{m}$ , and 6  $\mu\text{m}$ .



E4600

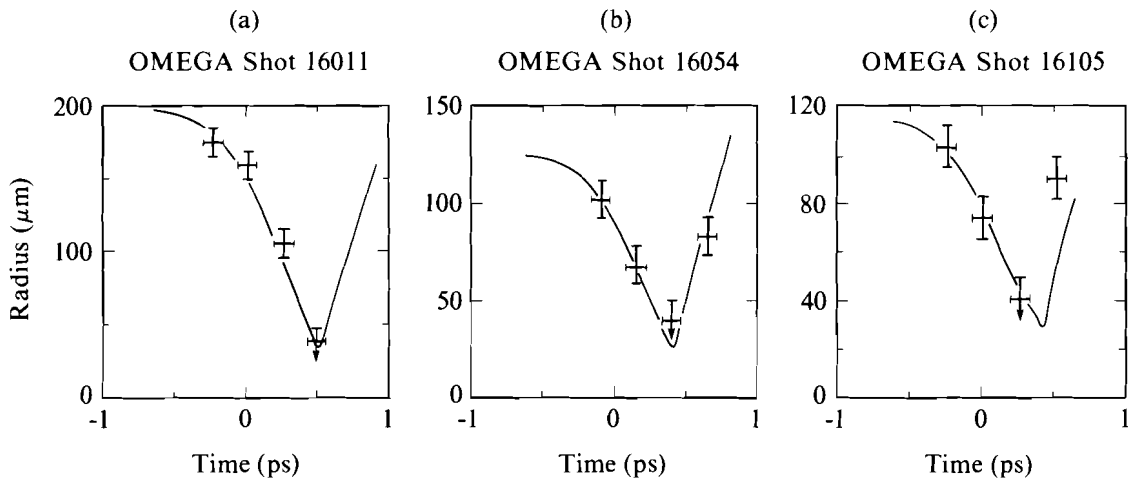
Fig. 35.4

X-ray images of a cryogenic target implosion taken with a four-frame x-ray-framing camera. The darker-shaded regions are the regions of highest x-ray emission. Small-scale structure is due principally to noise from the gated microchannel plate (MCP).

Further information about the implosion time history is obtained from measurements taken with the MINIFLEX soft x-ray photodiode system.<sup>15</sup> The MINIFLEX system consists of an array of four x-ray-sensitive photodiodes whose signals are read out by 3-GHz oscilloscopes, yielding spatially integrated, time-resolved ( $\sim 200$ -ps FWHM) measurements of the x-ray emission. Figure 35.6 shows the time-resolved x-ray emission observed with MINIFLEX for the three target experiments of Fig. 35.5, together with *LILAC* predictions of the same. The measured and predicted curves were compared by normalizing the heights of the broad peak in the emission curve (corresponding roughly to the peak of the laser pulse) and by assuming these peaks to coincide in time. We see with these assumptions that the times of the measured and predicted stagnation peaks (Fig. 35.6) are nearly coincident. However, the height of the measured stagnation peak appears to deviate more for the thicker-shelled targets.

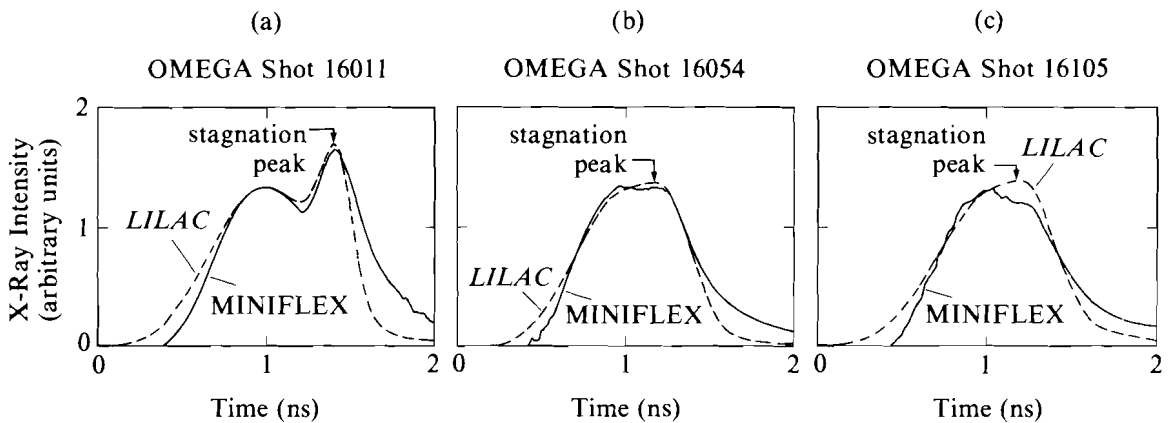
The size of the imploding shell as a function of time, as measured by the x-ray framing camera, and the time of shell stagnation, as measured by the MINIFLEX system, are in general agreement with the one-dimensional code predictions. The implosions are further diagnosed by analysis of high-resolution, hard x-ray images obtained





E4635

Fig. 35.5  
 Radius of peak x-ray emission versus time of three cryo targets having (a) 3- $\mu\text{m}$ , (b) 5- $\mu\text{m}$ , and (c) 6- $\mu\text{m}$  walls, determined from framed x-ray images and as predicted by *LILAC*.

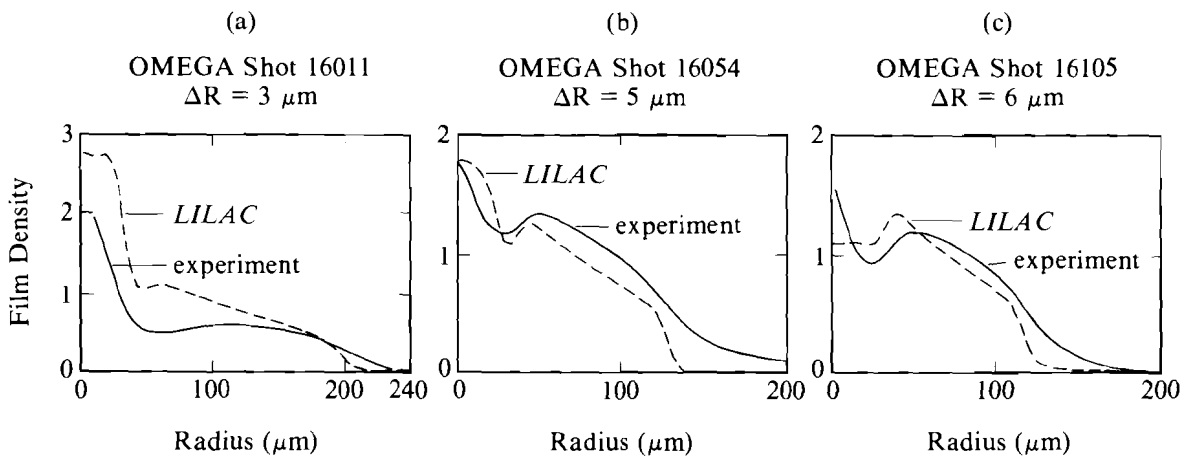


E4634

Fig. 35.6  
 Time-resolved spatially integrated x-ray fluence from cryo targets that have wall thicknesses of (a) 3  $\mu\text{m}$ , (b) 5  $\mu\text{m}$ , and (c) 6  $\mu\text{m}$ , and *LILAC* prediction of same.

with a Kirkpatrick-Baez (KB) microscope,<sup>16</sup> which has a resolution of  $\sim 5 \mu\text{m}$  and records images on x-ray-sensitive film. The effective-energy range sampled in these images is 3.0 to 4.6 keV, limited at the low-energy end by transmission of the x rays through a metallic filter and at the high-energy end by reflection off the KB mirrors. Figure

35.7 shows the average radial profiles determined from KB microscope images of the same target experiments analyzed in Figs. 35.5 and 35.6, and from predictions of the same. The high-density regions at the center of the images are due to the continuum-dominated flux generated by shell stagnation. The predicted profiles all contain an outer peak at a radius that corresponds to the radius of peak emission (roughly the shell radius at the time of the peak of the pulse). An inner peak is present on the predicted profiles of the two thinner-shelled targets [Figs. 35.7(a) and 35.7(b)] but not on the predicted profile of the thicker-shelled target [Fig. 35.7(c)]. This is because the optical depth of the material is predicted to be high enough to prevent it from being seen. The measured profiles show stagnation region features that are smaller in radius than predicted. The measured profile of the thick-shelled target shows a central peak where none is predicted.



E4632

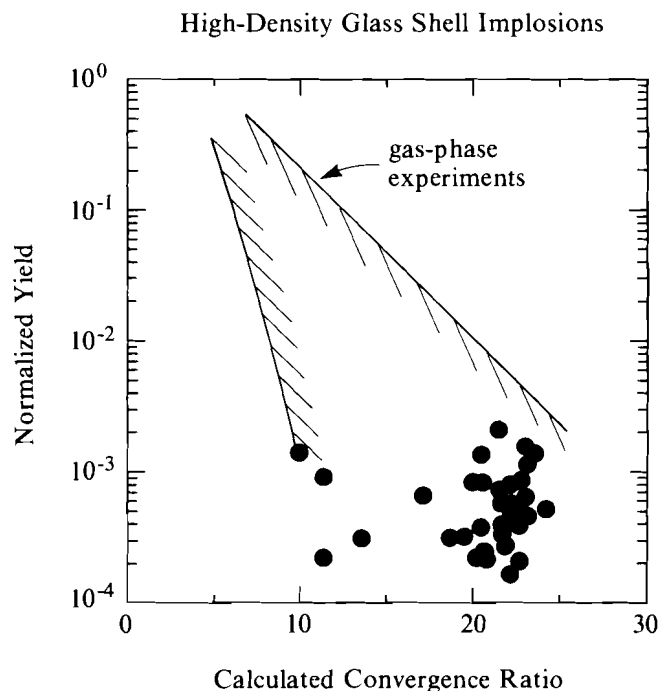
Fig. 35.7

Radial profiles determined from x-ray microscope images of cryo targets that have wall thicknesses of (a)  $3 \mu\text{m}$ , (b)  $5 \mu\text{m}$ , and (c)  $6 \mu\text{m}$ , and LILAC prediction of same.

## 2. Neutron Yield

The total thermonuclear yield  $Y_N$  was measured for these experiments by a Cu activation system, an Ag activation system, and an array of neutron scintillator-photomultiplier pairs.<sup>17</sup> All of these yield-measuring systems were cross calibrated to the Cu activation system, which was absolutely calibrated. Errors in the measured yield for these experiments were primarily due to counting statistics. Figure 35.8 shows the normalized neutron yield (the measured neutron yield divided by the calculated yield) plotted as a function of the calculated convergence ratio  $C_R$ . (The convergence ratio is defined as the initial fuel-pusher interface radius divided by the minimum fuel-pusher interface ratio.) The normalized yields range from  $\sim 3 \times 10^{-3}$  to  $\sim 1 \times 10^{-4}$ . The errors in the measured yield are, in general, much smaller than the scatter of the values. Previous measurements of the

Fig. 35.8  
Normalized neutron yield (ratio of experimentally measured yield to predicted yield) versus the calculated target convergence ratio (the ratio of the initial to final fuel-shell interface radius) for the cryogenic target experiments. The shaded region shows the range of normalized yields found for previous gas-phase experiments.



E4633

neutron yield produced by gas-phase targets illuminated by OMEGA<sup>18-20</sup> have shown that the normalized neutron yield is a decreasing function of  $C_R$ . In fact, the cryo experiments fall in the range of normalized yields observed for gas-phase target experiments (indicated by the shaded region in Fig. 35.8) where they overlap. The cryo targets, therefore, show normalized neutron yields that are similar to normalized yields observed from previous gas-phase target experiments, if targets having the same calculated convergence ratio are compared.

### 3. Fuel Areal Density

The fuel areal density  $\rho R$  at the time of neutron yield (neutron-averaged  $\rho R$ ) was measured by the "knock-on" diagnostic technique.<sup>21,22</sup> This technique measures the number of deuterons and tritons in the compressed fuel that are scattered by 14.1-MeV fusion neutrons, the number of such ions (knock-ons) being directly proportional to the  $\rho R$ . The ions were detected by stacks of polycarbonate (CR-39) track-detector foils, with metallic filters in front of and in between the foils. Three sets of knock-on detector foil-filter stacks were positioned at nearly mutually orthogonal positions around the target, both to increase the solid angle of the collector and to provide as representative a sample of the average knock-on flux as possible. Deuterons and tritons were distinguished from other particles (e.g., protons) by placing a criterion on the tracks left in the foils.

Only tracks with diameters exceeding a specified minimum diameter, which completely penetrated an individual foil, were counted as being left by knock-ons. These criteria limited the knock-ons detected in a single foil to a known, finite-energy window.<sup>21</sup>

The knock-on energy spectrum was sampled over a broad range by using metallic filters to slow down the knock-ons so that their energy was in the energy window defined by the track selection criteria. We used a stack of metallic filters and five CR-39 foils, which sampled the knock-on spectrum in five nearly independent energy intervals. We found that, although the position of the deuteron peak and hence the fraction of the total number of deuterons detected in any one foil differs depending on the amount of slowdown in the target, the sum of the knock-ons detected in four of the five foils is a nearly constant fraction,  $f_D = 0.085$ , to within  $\pm 5\%$ , for  $\rho R_{\text{total}} \leq 50 \text{ mg cm}^{-2}$  ( $\rho R_{\text{total}} = \rho R + \rho \Delta R$ ). This is an upper bound on  $f_D$ , which is independent of  $\rho R_{\text{total}}$ , temperature of the fuel, or the amount of fuel-shell mixing. (Further details of this analysis will be explained in an upcoming LLE Review article.) The fuel areal density was obtained from the number of detected deuteron tracks by

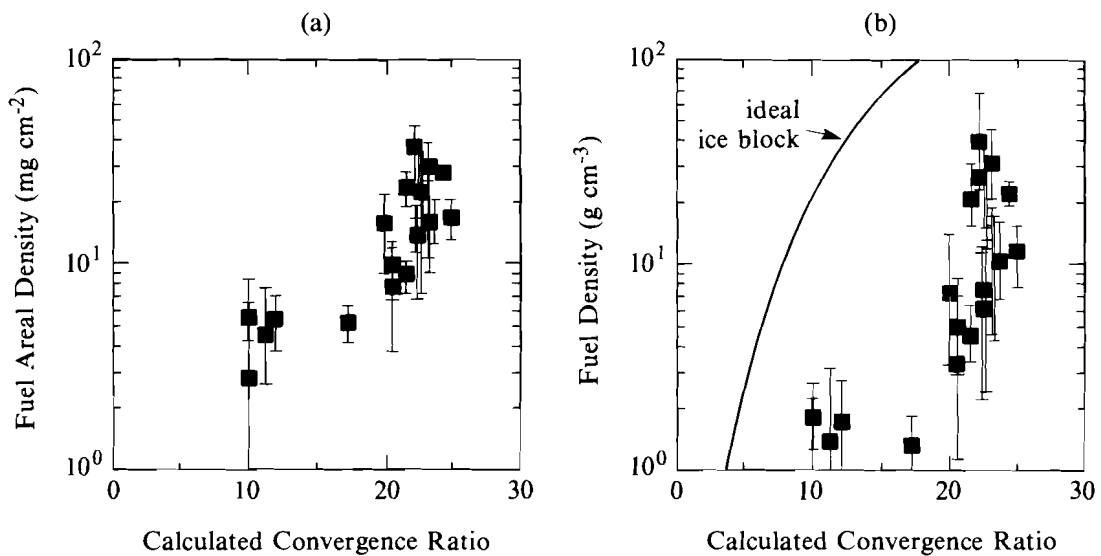
$$\rho R = 5.4 \times 10^3 \frac{K_D}{Y_N} \left( \frac{4\pi}{\Delta\Omega} \right) \frac{1}{f_D},$$

where  $K_D$  is the sum of the knock-on tracks detected in the four foils,  $\Delta\Omega$  is the solid angle subtended by the foils, and  $Y_N$  is the neutron yield. Since  $f_D$  appears in the denominator of this expression and we use an upper bound of its value, we are able to obtain a lower bound on  $\rho R$ .

Figure 35.9(a) shows the measured fuel areal densities plotted versus the calculated convergence ratios. (The error bars are calculated from the combined relative errors in measurement of the neutron yield and the knock-on flux.) The highest values of  $\rho R$  are in the range 20 to 35  $\text{mg cm}^{-2}$ , which were obtained by targets whose calculated convergence ratios are in excess of 20.

#### 4. Fuel Density

The fuel density averaged over the time of thermonuclear burn (neutron-averaged  $\rho$ ) can be estimated from the measured  $\rho R$  by assuming a simple model for the distribution of the fuel. One such model (the "ice-block" model) assumes that the fuel has a constant density and is compressed into a region of radius  $R$ , and that neutrons are produced at the center of this region.<sup>23</sup> Assuming that all of the initial mass of the fuel,  $M$ , is compressed into this region, then the fuel density can be expressed as  $\rho = (4\pi/3M)^{1/2} (\rho R)^{3/2}$ . Although this is a simple model that is not expected to accurately describe the actual fuel distribution, it does give a conservative estimate of the fuel density. As an example, if the neutron production were constant across the fuel volume, the resulting inferred density would be  $\sim 50\%$  higher than would be inferred by the ice-block model. The fuel densities inferred from the measured  $\rho R$ , using the ice-block model, are shown in Fig. 35.9(b). The highest inferred fuel densities are in the range of 20 to 40  $\text{g cm}^{-3}$  (100 to 200 XLD), again obtained with targets whose



TC2399

Fig. 35.9

(a) The measured fuel areal densities and (b) the inferred neutron-averaged fuel densities. The line in (b) indicates the maximum density that could be obtained for a given convergence ratio.

calculated convergence ratios are in excess of 20. The curve in Fig. 35.9(b) shows the density that would be obtained if all of the fuel were to be uniformly compressed to the calculated convergence ratio (assuming 100-atm initial fuel pressure).

### Discussion

The amount of energy absorbed by the cryo targets was measured and found to be in good agreement with the predicted absorbed energy (Table 35.I). The time history of the cryo target implosions was diagnosed by measurements of the shell size versus time determined from x-ray framing camera images and by measuring the time of shell stagnation from x-ray photodiode measurements. These measurements indicate that the cryo targets are imploding nearly as predicted by the one-dimensional code *LILAC*. The measured neutron yields [Table 35.I, col. 7(a)] and the measured fuel areal densities [Table 35.I, col. 8(a)], however, fall below the predicted values. It has been pointed out previously<sup>21</sup> that the falloff of neutron yield with an increasing convergence ratio could be explained by illumination nonuniformities of the OMEGA system. As is seen in Fig. 35.8, the cryo target experiments show a similar trend, indicating that their performance was degraded by a similar mechanism. Deviations of both the measured size of the x-ray stagnation peak (Fig. 35.6) and the shape of the emission from the stagnating core (Fig. 35.7) from predictions indicate that although the shell and fuel are reaching maximum compression when predicted, the shell and fuel may still not be integral. The illumination nonuniformities known to remain in the

OMEGA system may be causing early implosion of some shell material, mixing of shell material, and a subsequent reduction in neutron yield. If neutrons are generated earlier than predicted (for instance, by early stagnating material), then the fuel will have reached a substantially lower areal density [see Fig. 35.3(c)], since the fuel areal density is predicted to increase by more than an order of magnitude within a very short time ( $\sim 50$  ps). The critical timing of the neutron burst with respect to the time of peak density attainment may be the dominant effect explaining the scatter of the measured fuel areal densities versus the convergence ratio [Fig. 35.9(b)]. Or, if pusher material has mixed into the fuel, it is expected that the actual convergence ratio achieved would be lower than predicted, again resulting in lower measured and inferred densities.

### Summary

A series of direct-drive, ablatively driven implosion experiments were carried out on the 24-beam, 351-nm OMEGA laser system using cryogenic DT glass microballoons. Distributed phase plates were used to improve the target irradiation uniformity. Typical measured absorption fractions of 60% to 80% agreed with predicted values of this quantity. Time-resolved x-ray measurements showed that shell radius versus time and the time of shell stagnation were in good agreement with one-dimensional simulations. These results indicate that average features of the implosions are being accurately modeled by one-dimensional simulations.

Deviations from one-dimensional performance were seen in the shapes of the x-ray-emitting regions of the stagnating shell material, the height of the x-ray stagnation peak, the neutron yield, and the fuel areal density. It is likely, although not certain, that these effects result from nonuniform implosion of fuel and shell material due to residual nonuniformities in the OMEGA laser irradiation on target. Nevertheless, fuel areal densities of 20 to 35 mg cm<sup>-2</sup> were measured using the knock-on diagnostic technique, implying neutron-averaged fuel densities of 20 to 40 g cm<sup>-3</sup> (100 to 200 XLD). These experiments have resulted in the first direct measurements of the fuel areal density of highly compressed fusion fuel that do not involve any assumptions about temperature or fuel-shell mixing. The inferred fuel densities are the highest attained for any direct-drive laser-fusion experiments.

### ACKNOWLEDGMENT

This work was supported by the U.S. Department of Energy Office of Inertial Fusion under agreement No. DE-FC08-85DP40200 and by the Laser Fusion Feasibility Project at the Laboratory for Laser Energetics, which has the following sponsors: Empire State Electric Energy Research Corporation, New York State Energy Research and Development Authority, Ontario Hydro, and the University of Rochester. Such support does not imply endorsement of the content by any of the above parties.

### REFERENCES

1. R. S. Craxton, R. L. McCrory, and J. M. Soures, *Sci. Am.* **255**, 68-79 (1986).
2. R. L. McCrory, J. M. Soures, C. P. Verdon, P. Audebert, D. Bradley, J. Delettrez, R. Hutchison, S. D. Jacobs,

- P. Jaanimagi, R. Keck, H. Kim, J. Knauer, R. Kremens, S. Letzring, F. Marshall, P. McKenty, M. C. Richardson, A. Simon, R. Short, S. Skupsky, and B. Yaakobi, *High-Intensity Laser-Matter Interactions* (SPIE, Bellingham, WA, 1988), Vol. 913; Laboratory for Laser Energetics Annual Report-1987, DOE/DP 40200-64, 93 (1988).
3. J. Nuckolls, L. Wood, A. Thiessen, and G. Zimmerman, *Nature* **239**, 139 (1972).
  4. R. F. Kidder, *Nucl. Fusion* **16**, 3 (1976).
  5. Laser Program Annual Report-1984, Lawrence Livermore National Laboratory, Livermore, CA, UCRL-50021-84, 5-35 (1985)
  6. S. D. Jacobs, K. A. Cerqua, T. J. Kessler, W. Seka, and R. Bahr, in 16th Annual Symposium on Optical Materials for High Power Lasers, *Nat. Bur. Stand. (U.S.), Spec. Publ. 727* (GPO, Washington, DC, 1986), p. 15.
  7. LLE Review **33**, 1 (1987).
  8. LLE Review **31**, 106 (1987).
  9. LLE Review **33**, 11 (1987).
  10. D. L. Musinski, T. M. Henderson, R. J. Simms, and T. R. Pattinson, *J. Appl. Phys.* **51**, 1394 (1980).
  11. B. I. Bennett, J. D. Johnson, G. I. Kirley, and G. T. Rand, Los Alamos National Laboratory Report No. LA-7130, 1978.
  12. W. F. Huebner, A. L. Merts, N. H. Magee, Jr., and M. F. Argo, Los Alamos National Laboratory Report No. LA-6760-M, 1977.
  13. LLE Review **31**, 101 (1987).
  14. J. D. Kilkenny, P. Bell, R. Hanjks, G. Power, R. Turner, J. Weidwald, and D. K. Bradley, *Rev. Sci. Instrum.* (to be published).
  15. G. Pien, M. C. Richardson, P. D. Goldstone, R. H. Day, F. Ameduri, and G. Eden, *Nucl. Instrum. Methods* **B18**, 101 (1986).
  16. M. C. Richardson, G. G. Gregory, R. L. Keck, S. A. Letzring, R. S. Marjoribanks, F. J. Marshall, G. Pien, J. S. Wark, B. Yaakobi, P. D. Goldstone, A. Hauer, G. S. Stradling, F. Ameduri, B. L. Henke, and P. A. Jaanimagi, in *Laser Interaction and Related Plasma Phenomena, Vol. 7*, edited by H. Hora and G. H. Miley (Plenum Press, New York, 1986), p. 179.
  17. M. C. Richardson, R. F. Keck, S. A. Letzring, R. L. McCrory, P. W. McKenty, D. M. Roback, J. M. Soures, and C. P. Verdon, *Rev. Sci. Instrum.* **57**, 1737 (1986).
  18. LLE Review **28**, 155 (1986).
  19. LLE Review **31**, 93 (1987).
  20. LLE Review **25**, 7 (1985).

21. S. Kacenjar, L. M. Goldman, A. Entenberg, and S. Skupsky, *J. Appl. Phys.* **56**, 2027 (1984).
22. S. Skupsky and S. Kacenjar, *J. Appl. Phys.* **52**, 2608 (1981).
23. E. M. Campbell, W. M. Ploeger, P. H. Lee, and S. M. Lane, *Appl. Phys. Lett.* **36**, 965 (1980).

## 1.B Effect of Barrier Layers on Burn-Through Time in Parylene

Burn-through experiments have the potential of providing a measure of the quality of laser illumination uniformity. In these experiments, the laser irradiates a spherical target consisting of an inner substrate shell, sometimes covered with a thin signature layer of a moderate-Z material such as Al, coated with a parylene (CH) layer of varying thickness. Nonuniformities in the laser illumination result in different burn-through times through the CH layer; in particular, the shortest burn-through time can be associated with the highest intensities present at the target surface. This effect was first observed in transport experiments carried out on the OMEGA laser system,<sup>1</sup> in which the burn-through time through a layer of CH overcoating a glass sphere was measured using the time-resolved spectrometer SPEAXS.<sup>2</sup> The results could only be modeled by assuming that a small fraction of the laser energy (<10%) was present at two to three times the nominal laser irradiance ( $I_0$ , defined as the laser power divided by the target surface area). It was supposed that small hot spots (<20  $\mu\text{m}$ ) were responsible for the large burn-through rates. Subsequent modeling of the laser far-field distribution has shown that small phase errors present in the beam before the focusing lens produced such hot spots.<sup>3</sup> Thus, while burn-through experiments cannot provide a full measure of the illumination uniformity, they can indicate the presence and the approximate magnitude of hot spots in the illumination pattern at the target surface.

Qualitative conclusions on the maximum intensity of the hot spots depend on the assumption that no other processes exist that can lead to fast burn-through signals. This assumption was questioned in further experiments that were carried out, after modifications to the laser system, to study the effect of barrier layers on the penetration of hot spots. Barrier layers are thin (<0.1- $\mu\text{m}$ ) layers of medium- to high-Z material coated on the outside of the target. The burn-through rates measured in these experiments were faster than those measured in previous experiments;<sup>4</sup> almost ten times the nominal irradiance was required to replicate the measured burn-through rates in bare (uncoated) CH. On the other hand, the addition of a thin Al barrier layer (0.1  $\mu\text{m}$ ) resulted in a burn-through rate similar to those observed previously. Figure 35.10 illustrates the results: the ablated areal density was obtained from targets with increasing thicknesses of CH. The ablated areal density for the bare CH increases very sharply and shows no sign of flattening like the simulation curves.



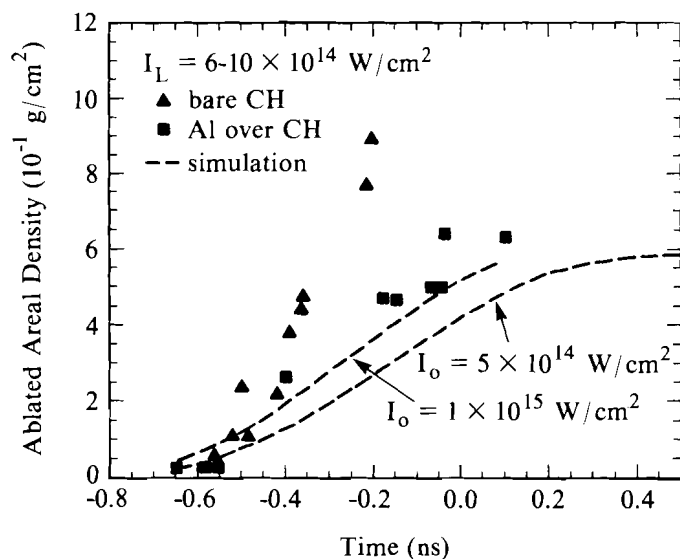


Fig. 35.10

Comparison of the burn-through times for CH layers of varying thickness, with and without an Al barrier layer, for the experiment that prompted the study of the effect of various barrier layers on the burn-through time.

TC2230

It was difficult, at this point, to attribute these large burn-through rates solely to hot spots with intensity larger than ten times the nominal intensity profiles. Several other processes were then proposed to explain the cause of this large burn-through and the effect of adding an outer layer of Al. The processes considered were (1) hot spots of intensities exceeding ten times nominal; (2) shine-through of the laser light early in the pulse while CH is still transparent; (3) a prepulse that would ablate part of the bare CH layer; and (4) filamentation and self-focusing of the hot spots.

These processes are discussed below. Several of them can be eliminated based on the requirement that the addition of a thin Al barrier layer strongly affects the burn-through time. Others required further experiments, which will be described after the discussion of the processes.

Two effects can result from the presence of hot spots: an enhanced penetration of the heat front, and hole drilling, which brings laser-heated material in contact with colder surrounding material, including the signature-layer material (see Fig. 35.11). Simulations of the burn-through experiment using the one-dimensional code *LILAC* indicate that hole drilling does not lead to earlier burn-through than the enhanced penetration of the heat front. There are two difficulties with using hot spots as an explanation for the observed burn-through rates: x-ray and equivalent-target-plane imaging do not show the presence of hot spots with intensities ten times nominal, and one-dimensional hydro simulations indicate that, because the laser burns through a  $0.1\text{-}\mu\text{m}$  layer of Al about 700 ps before the peak of the pulse, such a

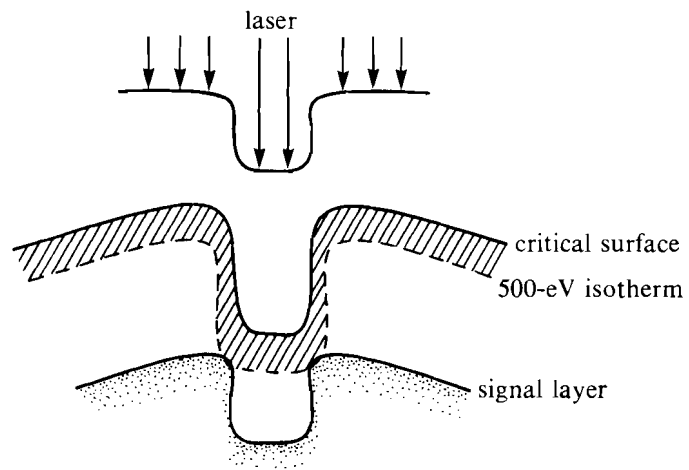


Fig.35.11  
Schematic description of hot-spot drilling. A hot spot in the laser beam can effectively drill a hole in the plastic because of the lack of smoothing for 350-nm laser illumination. X-ray emission from the barrier layer can occur when the edge of the heat front around the hole reaches the signal layer.

layer cannot be expected to smooth out the hot spots. Simulations also indicate that a thin barrier layer does not affect hole drilling.

The second process considered, shine-through, assumes that because CH is transparent to UV light at room temperature laser light would penetrate to the signal layer early in the pulse and heat it. This process is very attractive because it would directly explain the effect of adding a thin barrier layer of aluminum. Shine-through was studied using *LILAC*. In the cold target, the laser light was deposited at the boundary of the CH and signal layers. As the electron temperature increased from thermal conduction, in the region immediately in front of the deposition region, the CH became ionized and a critical surface was created: the laser light was then deposited in the zone where the electron temperature reached 1 eV (varying this threshold temperature made little difference). This caused an ionization wave to propagate quickly from the signal layer to the target surface. At that point, the CH layer was a slowly expanding plasma with temperatures of a few electron volts and a density slightly below solid. As the laser energy increased in time, an ablation surface was quickly established and the plastic layer was recompressed to conditions very near those obtained in the absence of shine-through. As a result, burn-through times were not affected by shine-through. Another possible effect of shine-through is that a nonuniform energy deposition at the CH-signal-layer interface may lead to a nonuniform low-density plasma in the CH layer by the time the ablation surface is established. These conditions may seed the Rayleigh-Taylor instability during the recompression, which may lead to mixing of signal layer material into the CH layer. This process is being studied with the two-dimensional hydrocode *ORCHID*.

The presence of a laser prepulse is also an attractive explanation because the burn-through rates increased after changing the oscillator

and removing the prepulse suppressor in the OMEGA laser system. A prepulse absorbed on or close to the surface of the target would have the effect of removing target material before the arrival of the main pulse. As such, the presence of a 0.1- $\mu\text{m}$  Al barrier layer should not make any difference. Also, it can be estimated from Fig. 35.10 that about 4  $\mu\text{m}$  of CH would have to be ablated off by the prepulse to bring the 8- $\mu\text{m}$  burn-through time for the bare CH target in line with the time for the Al-coated target. Ablating 4  $\mu\text{m}$  of plastic requires about 600 J of energy, which is far more than can be delivered by a prepulse. On the other hand, combining a prepulse with shine-through can, in theory, lead to an early burn-through signal. A prepulse could be generated 7 ns before the main pulse if the previous pulse in the oscillator were not suppressed properly. When such a prepulse is deposited at the signature and CH-layers interface, it causes the plastic layer to expand slowly until the main pulse arrives. At that point, the plastic directly in front of the interface has decompressed to densities a few percent of solid. As the main laser pulse establishes a strong ablation front, it sends a shock that recompresses that material. The recompression can heat the CH and a thin layer of the signal layer next to the interface up to 200 eV, which is enough to produce the observed early onset of the x-ray emission. A prepulse energy in excess of 100 mJ is required to produce the needed x-ray emission. Subsequent monitoring by the laser group has established that, if a 7-ns prepulse existed, its energy would be  $<1$  mJ. Therefore, the existence of a prepulse must be ruled out as a cause of early burn-through.

Finally, filamentation and self-focusing could be responsible for the observed fast burn-through times. Both processes can lead to local laser intensities larger than those applied to the target and therefore to a higher estimate of the maximum intensity in the laser illumination. A distinction is made here between the two processes: filamentation arises from initial small perturbations in the laser illumination and is calculated from a linear perturbation of the light-wave equation; whereas self-focusing involves the entire beam (or a hot spot treated as a beam) and is treated by solving the paraxial equation for a Gaussian beam propagating in a medium. The two processes are, of course, driven by the same mechanism: regions of higher laser intensities give rise to regions of lower electron densities in the plasma into which the laser light is refracted because of the lower index of refraction, creating even higher local intensities. These processes are divided into two types, ponderomotive and thermal, depending on whether the plasma is forced out of the high-intensity region by the ponderomotive force of the laser light, or by the high pressures resulting from high temperatures. Filamentation and self-focusing can occur in the corona at all times, although a minimum-beam radius is usually associated with self-focusing. Even though threshold intensities are quoted in the literature for the onset of filamentation and self-focusing, a better criterion to judge their importance is to compare the filamentation and self-focusing growth lengths with the available plasma scale length, i.e., the two processes need enough plasma to develop and focus the light to high intensities. The growth-length scalings found in the literature are obtained from simple models that assume uniform

plasmas and neglect laser-light absorption and heat conduction. Results are not available from code simulations of thermal filamentation or self-focusing under the experimental conditions that apply here: a subnanosecond laser pulse illuminating a solid plastic pellet. Two-dimensional simulations of ponderomotive effects are practically nonexistent because the steep gradients and very short scale lengths generated in the plasma require an extremely fine resolution and, therefore, too many computational zones.

The growth lengths for ponderomotive and thermal filamentation are given, respectively, as the axial wave number of the fastest-growing mode:<sup>5</sup>

$$k_p = \frac{1}{8} \left( \frac{v_0}{v_{th}} \right)^2 \frac{\omega_{pe}}{k_0 c^2}$$

and

$$k_{th} = \frac{\omega_{pe}}{7.5 k_0 c} \frac{v_0}{v_{th}} \frac{1}{\lambda_{ei}},$$

where  $v_0$  is the quiver velocity,  $v_{th}$  the thermal velocity,  $\omega_{pe}$  the plasma frequency,  $k_0$  the laser wavenumber, and  $\lambda_{ei}$  the electron-ion collision frequency. Note that the ponderomotive growth length is independent of the  $Z$  of the material. For the conditions of interest at the time of the burn-through in the CH layer,  $T_e = 1$  keV,  $I = 1 \times 10^{14}$  W/cm<sup>2</sup>; for  $n_c/n_e = 10$ , the ponderomotive growth length is about 2 cm and the thermal growth length about 0.16 cm. While estimates of these growth lengths may vary (for example, another estimate<sup>6</sup> yields about 0.1 cm and 600  $\mu$ m for the ponderomotive and thermal filamentation growth lengths, respectively), the growth lengths exceed by about one or more orders of magnitude the distance between tenth-critical and critical surfaces at burn-through time (see Fig. 35.16, used in a later discussion).

The growth lengths for self-focusing are more difficult to obtain, but a rough estimate of the ponderomotive growth length is available.<sup>7</sup> The ponderomotive self-focusing distance is given by

$$R_p = \sqrt{3} r_0 \frac{\omega}{\omega_{pe}} \left( 1 - \frac{n_e}{n_c} \right)^{1/2} \frac{v_{th}}{v_0},$$

where  $r_0$  is the beam or hot-spot radius,  $\omega$  the laser frequency, and  $n_e/n_c$  the ratio of the electron density to the critical density. For the conditions described above, we get  $R_p = 3.5 r_0$ , or, for a 20- $\mu$ m hot spot,  $R_p = 35 \mu$ m. It is therefore possible for hot spots with intensity two or three times nominal to self-focus and to produce intensities ten times nominal. However, it is difficult to imagine how the presence of a 0.1- $\mu$ m barrier layer of aluminum could affect self-focusing, since such a layer is ablated about 500 to 600 ps before the burn-through time for 6  $\mu$ m of bare plastic.

With none of the proposed processes able to explain the fast burn-through rate, it was decided to conduct experiments in which the plastic layer was overcoated with barrier layers of varying materials and thicknesses; of particular interest were transparent materials with a  $Z$  higher than CH. The targets consisted of thick glass shells covered with a  $0.1\text{-}\mu\text{m}$  signal layer of Al, a  $6\text{-}\mu\text{m}$ -thick layer of CH, and a barrier layer with materials and thicknesses as listed in Table 35.II. These targets were irradiated by the OMEGA laser system at  $351\text{ nm}$  with  $600\text{-ps}$  FWHM pulses and an irradiance of  $8 \times 10^{14}\text{ W/cm}^2$ . The beams were focused tangentially to the targets to provide good overall uniformity and absorption. The burn-through time was measured with SPEAXS from the onset of the signal-layer emission. An absolute timing reference to the incident laser pulse was provided by a separate UV fiducial signal.<sup>8</sup>

Table 35.II

Onset times of the x-ray emission from the signature layer for the various barrier layers and the intensity required in simulations to match the measured burn-through times.

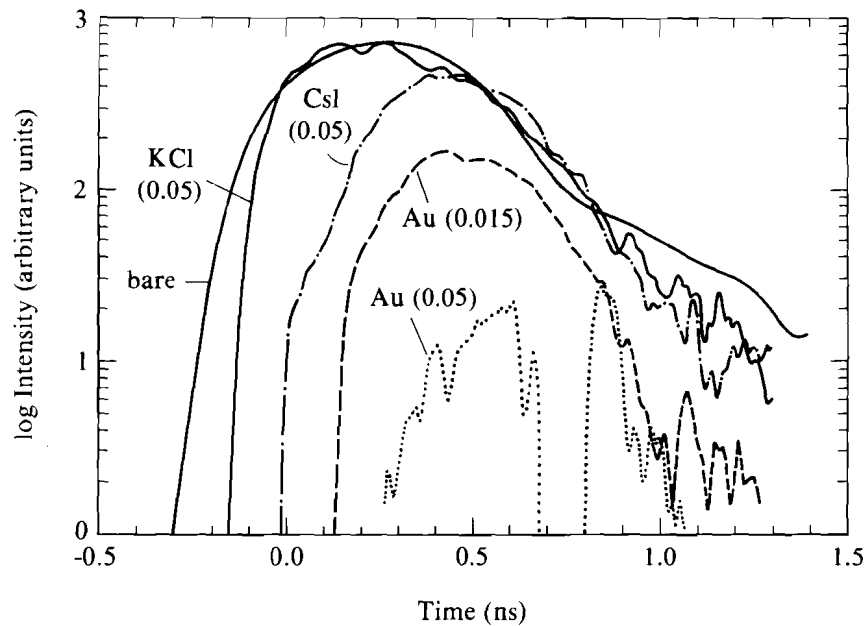
Material	Thickness ( $\mu\text{m}$ )	$Z$	Time (ps)	$I_s^* / I_0$
bare	—	—	$-250 \pm 20$	$12 \pm 1.7$
Al	0.1	13	$-25 \pm 20$	$4.2 \pm 1.2$
KCl	0.1	18	$-150 \pm 20$	—
CsI	0.05	54	$0 \pm 20$	$4.1 \pm 2.0$
Au	0.015	79	$125 \pm 20$	$2.1 \pm 0.2$
Au	0.05	79	$350 \pm 50$	1.5

\* $I_s$  is the intensity required in simulations to match the measured burn-through times.

TC2396

The temporal emissions of the Al H- $\alpha$  for the set of targets are shown superposed in Fig. 35.12; the continuum has been subtracted and time is with respect to the peak of the pulse. The burn-through time for the bare CH target (areal density of  $6 \times 10^{-4}\text{ g/cm}^2$ ) is the same as that obtained in Fig. 35.10. With one exception—KCl—as the average  $Z$  of the outer layer material is increased from 3.5 (bare CH) to 79, the burn-through time increases; the results are summarized in Table 35.II. Again, for an Al barrier layer, the burn-through time of Fig. 35.10 is recovered. KCl, the exception, has an earlier time than Al, even though the two materials have the same  $Z$  and KCl is slightly lighter than Al. Also, increasing the thickness of the Au layer also increases the burn-through time; for  $0.05\text{ }\mu\text{m}$  of gold, the burn-through is marginal.

To determine whether the change in burn-through time is due only to the added mass of the barrier layer and energy loss to x-ray radiation in the high- $Z$  layer, simulations were performed with *LILAC*. Included in *LILAC* for these simulations, instead of the tabular local thermal equilibrium (LTE) ionization levels and opacities, is a non-LTE



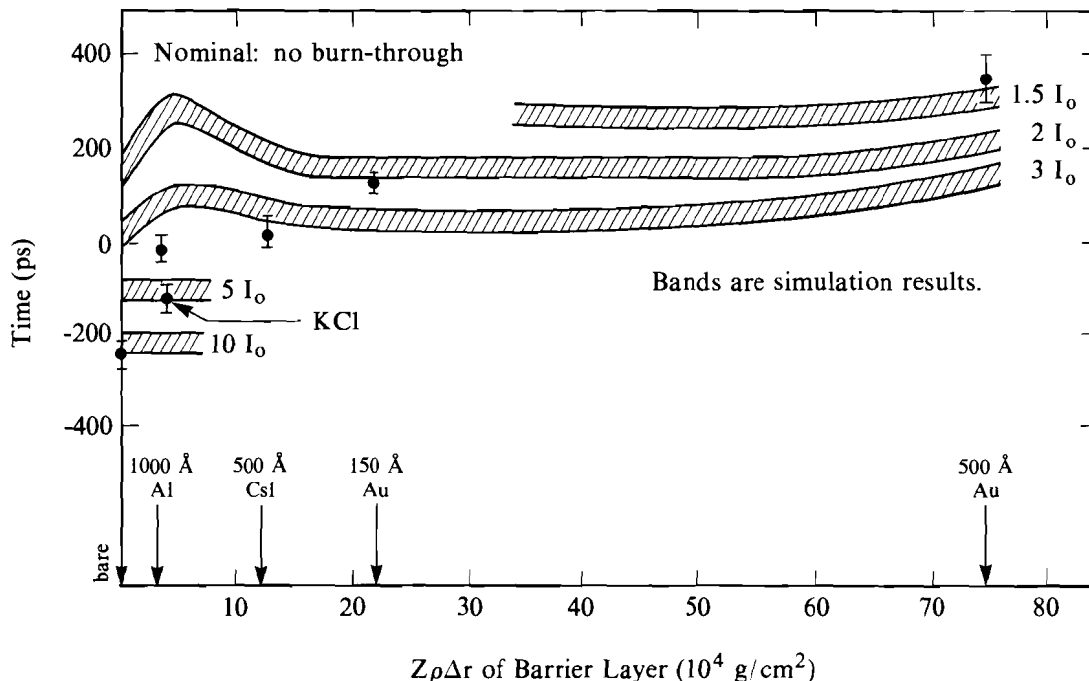
E4645

Fig. 35.12

Emission from the signal layer for the various barrier layers. The time is with respect to the laser pulse; the continuum has been subtracted.

average-ion model<sup>9</sup> that provides a better description of the ionization and radiation processes in high-Z material. Each of the cases was first run at nominal intensity, and then at progressively higher intensities until the burn-through time matched the measured time.

The results are shown in Fig. 35.13, where the burn-through time is plotted against the product of the average  $Z$  of the material and the areal density of the barrier layer. This scaling is not based on any particular physical basis, but is an attempt to include both the effect of the increasing  $Z$  and of the varying density and thicknesses of the barrier layer material. Of interest is that the experimental points for the nontransparent barrier layers, when scaled in this manner, are nearly linear with burn-through time. The burn-through times from simulations, on the other hand, do not show such a dependency on the material within the range of  $Z$  and thicknesses used in the experiment (some variations are due to differences in laser intensity in the shots). The burn-through time is slightly longer for Al than for bare CH, CsI, and thin Au. The mass of the CsI layer is about half of the other two. This added mass, and the radiated x-ray energy, should lead to slightly longer burn-through times for these targets than for the bare-CH target. The difference between the Al case and the two others is that the CsI- and Au-coated targets absorb more energy early in the laser pulse than does the Al-coated target, which compensates for the added mass. The longer burn-through time for the thick Au barrier layer is due to the higher mass of that layer and the x-ray radiation losses.



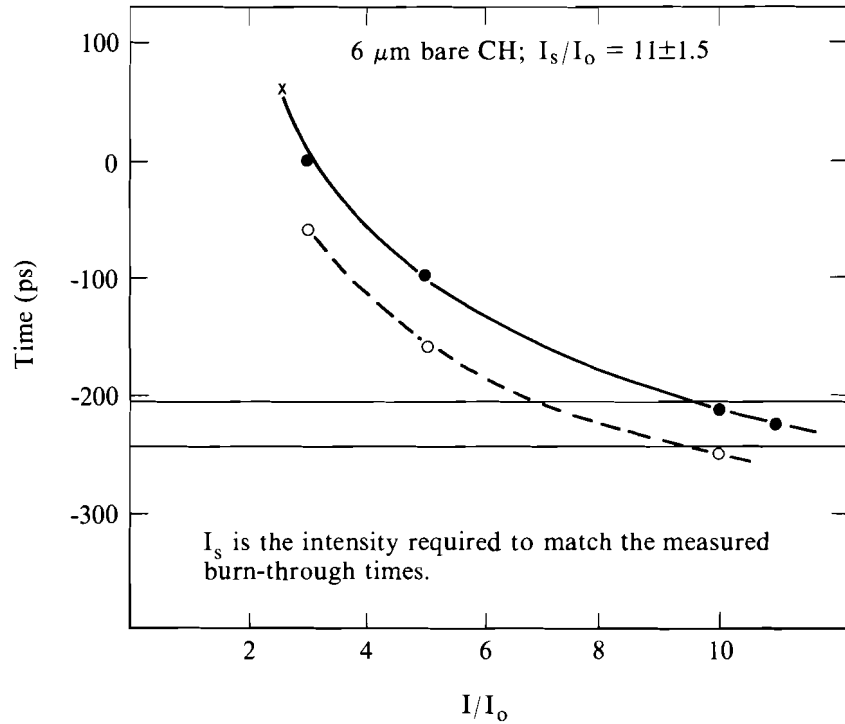
TC2397

Fig. 35.13

Burn-through time for the barrier-layer targets. The horizontal scaling has no physical significance. The points are the experimental results; the bands are the simulation results at various laser intensities. There is no burn-through in simulations at nominal intensity.

Table 35.II summarizes the experimental results and gives the intensities  $I_s$  (normalized to the nominal intensity) that are required in the simulations to match the measured burn-through times. Figure 35.14 shows the scaling of the burn-through time with intensity for the bare target and for the Al and CsI barrier-layer targets. Again, this figure shows how much shorter the measured burn-through time for the bare-CH target is compared to the simulation results; in the simulation, the scaling is similar for all three targets.

The results from this experiment confirm those shown in Fig. 35.10. About ten times nominal intensity is required to obtain the burn-through time for targets without barrier layers and about four times nominal intensity when a barrier layer of Al or CsI is added. The CsI barrier layer is lighter than the Al layer, but it has a higher  $Z$ , which seems to lead to a similar behavior. On the other hand, the thin Au layer, which has the same mass as the Al layer but a higher  $Z$  than the CsI layer, needs a lower laser intensity to match the experimental burn-through time. Finally, for the thicker Au barrier layer, there is almost agreement at nominal intensity with the experiment. Therefore, both the mass and the average  $Z$  seem to affect the processes responsible for the fast burn-through. The KCl barrier layer, which has almost the same mass and  $Z$  as Al, does not fit with the others.



E4625

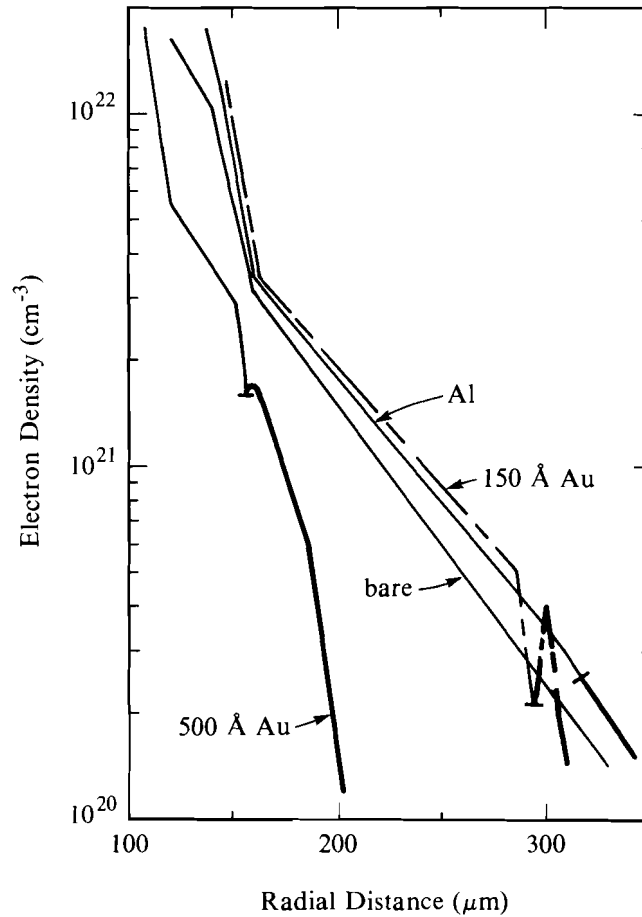
Fig. 35.14

Dependence of the burn-through time on the laser intensity for the bare-CH target and for targets with an Al and CsI barrier layer. The horizontal bands are the experimental times from Fig. 35.12.

The difference between KCl and the other materials is that it is transparent at room temperature (CsI is also transparent at room temperature, but its use as a photocathode material implies that free electrons can be created very quickly by the laser pulse). In a sense, KCl seems to behave partly as CH and partly as an opaque conductor, which indicates that early transparency is still important.

At this point, it appears that this new series of experiments, while providing more data on the problem, has not led to an understanding of the processes that cause the fast burn-through rates through CH. Both the KCl results and the effect of adding a barrier layer of Al on the burn-through time indicate that transparency at room temperature is important. Yet one-dimensional simulations do not show any difference in target behavior due to early shine-through, and measurements have not detected prepulse levels above the expected pulse shape. Another observation is that the thickness and the kind of nontransparent material used in the barrier layer make a difference: thick gold is more effective than thin gold, which in turn is more effective than an equivalent mass of aluminum. This suggests that such processes as self-focusing or radiation smoothing of the hot spots may be present. To appreciate the effectiveness of these processes, conditions in the corona 300 ps before the peak of the pulse are plotted in Fig. 35.15 for four barrier-layer cases at nominal intensity (as a reminder, the observed burn-through in bare CH is -250 ps; in the thin Au, 125





TC2377

Fig. 35.15  
 Calculated density profiles in the corona 300 ps before the peak of the pulse for four targets at nominal intensity: bare CH, 0.1  $\mu\text{m}$  of Al, 0.015  $\mu\text{m}$  of Au, and 0.05  $\mu\text{m}$  of Au barrier layers. The thicker part of the profile shows where the barrier-layer material is present. At this time, the nominal laser intensity is  $4.7 \times 10^{14}$  W/cm<sup>2</sup> and the laser intensity at 0.1 critical is  $2.0 \times 10^{14}$  W/cm<sup>2</sup>.

ps). At that time, the Al and thin Au barrier layers are far in the blowoff, at densities below 0.01 critical density, where their x-ray radiation efficiency is low; radiation smoothing, therefore, should not be important. The thick Au barrier layer is still present at densities about one-tenth critical density, and it is possible that the Au layer could still radiate enough to smooth out illumination nonuniformities. If radiation smoothing did exist, the effect of the thick Au layer would be to retard the effect of nonuniformity on the burn-through time by keeping the near-critical region smooth for a longer time early in the pulse. The difference between the results for Al and the thin Au layers cannot be similarly explained because both barrier layers are ablated at the same time.

The effectiveness of self-focusing depends on the scale lengths in the corona (ponderomotive self-focusing does not depend on the  $Z$  of the material). Figure 35.15 shows that, 300 ps before the peak of the pulse, the scale lengths for bare CH and for the Al and thin Au layers

are almost the same; for the thick Au layer, the scale lengths are shorter than for the other layers because the quarter-critical surface has barely burnt through the Au layer. The distance between the critical surface and the one-tenth critical surface, where self-focusing is more likely to occur, is plotted in Fig. 35.16 as a function of time. As the target outer material changes from CH to aluminum to gold, this distance is shorter early in the pulse, reflecting the steepening of the scale length as the  $Z$  of the material increases. But, after the one-tenth critical surface has burnt through the barrier layer, the effect is reversed and the scale lengths are longer for the higher- $Z$  cases. This may be caused by early radiation preheat, which heated the cold CH, creating a somewhat larger mass-ablation rate later in the pulse.

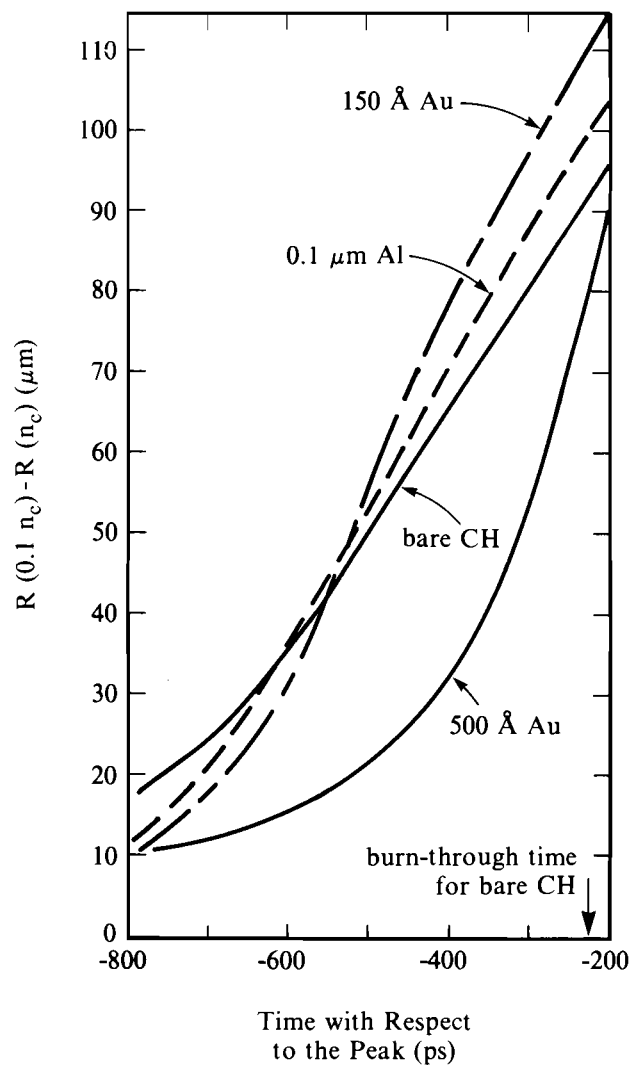


Fig. 35.16  
Temporal evolution of the distance between the 0.1-critical density surface and the critical density surface for the four targets described in Fig. 35.15. Time is with respect to the peak of the pulse.

TC2375

Despite these differences, the distances between the two surfaces for CH, Al, and thin Au are the same within less than 10  $\mu\text{m}$ ; only in the thick Au case are the distances much shorter. Thus, if self-focusing were occurring, it should be no different for the bare, Al, and thin Au cases; this is especially true since, as early as 300 ps before the peak of the pulse, these layers are below one-tenth critical and should not affect self-focusing between that surface and the critical surface. In fact, because self-focusing grows rapidly (the sound speed is large and the distances involved are of the order of 10 to 50  $\mu\text{m}$ ), it is doubtful that self-focusing could even explain the difference in the burn-through time between the thin and thick gold barrier layers.

### Summary

In conclusion, experiments with barrier layers consisting of different materials and thicknesses have been carried out in an attempt to understand the processes that cause the large burn-through in CH. The results show that burn-through occurs progressively later during the pulse as the barrier layers change from none, to aluminum, to thin gold, and to thick gold. Simulation results predict that there should be only small differences ( $< 100$  ps) in the burn-through time for all the barrier layers. Several processes, which could lead to fast burn-through rates, were studied: severe hot spots (intensities ten times nominal), shine through, the presence of a prepulse, and filamentation and self-focusing. None of these processes by itself could adequately explain the experimental results because measurements did not show their existence (severe hot spots, prepulse), because they were unaffected by the barrier layers (hot spots, self-focusing), or because one-dimensional simulations showed they had little effect (shine-through). It is very likely that different processes may be responsible for the differences in burn-through time for the various barrier layers: for example, the effect of the aluminum barrier layer and the fast burn-through with a KCl layer support early pulse shine-through; the effect of the thick gold layer gives an indication of early radiation smoothing. Prepulses, filamentation, and self-focusing are the least likely to explain any the observations. The possibility that nonuniform shine-through may cause the layers to become Rayleigh-Taylor unstable is being studied. More experiments are planned to understand the role of each of these processes.

### ACKNOWLEDGMENT

This work was supported by the U.S. Department of Energy Office of Inertial Fusion under agreement No. DE-FC08-85DP40200 and by the Laser Fusion Feasibility Project at the Laboratory for Laser Energetics, which has the following sponsors: Empire State Electric Energy Research Corporation, New York State Energy Research and Development Authority, Ontario Hydro, and the University of Rochester. Such support does not imply endorsement of the content by any of the above parties.

### REFERENCES

1. P. A. Jaanimagi, J. Delettrez, B. L. Henke, and M. C. Richardson, *Phys Rev. A* **34**, 1322 (1986).
2. B. L. Henke and P. A. Jaanimagi, *Rev. Sci. Instrum.* **54**, 1311 (1983).
3. LLE Review **31**, 106 (1987).

4. D. Bradley, 16th Annual Anomalous Absorption Conference (1987).
5. W. L. Kruer, *Comments Plasma Phys. & Controlled Fusion* **2**, 139 (1985).
6. LLE Review **28**, 164 (1986).
7. C. E. Max, *Phys. Fluids* **19**, 74 (1976); M. S. Shoda, A. K. Ghatak, and V. K. Tripathi, *Progress in Optics, Vol. XIII*, edited by E. Wolf (North-Holland, Amsterdam, 1976), p. 171.
8. P. A. Jaanimagi, L. DaSilva, G. G. Gregory, C. Hestdalen, C. D. Kiikka, R. Kotmel, and M. C. Richardson, *Rev. Sci. Instrum.* **57**, 2189 (1986).
9. R. Epstein (private communication).

### 1.C Barrier-Layer Experiments and Initial Plasma Formation in Laser Plasma

The initial phases of plasma generation on the surface of transparent solid targets under high-intensity laser irradiation are not very well understood. The problem is exemplified by the anomalous burn-through speeds obtained from x-ray spectra of multilayered targets. Those data have shown that the outer plastic (CH) layers always burn through at rates much too high to be accounted for on the basis of hydrodynamics and/or beam nonuniformities.<sup>1</sup> Similarly, experiments where a high-intensity laser beam was focused on the surface of a transparent Lucite block showed evidence of self-focusing filaments in the bulk of the material,<sup>2,3</sup> which was identified as light leakage during the early part of the evolution of the laser pulse, before an absorbing plasma was formed on the surface. In all cases, a relatively thin metal layer the thickness of a few hundred angstroms reduces the x-ray burn-through rates to near nominal levels and eliminates the visible filaments protruding into the Lucite after irradiation. Qualitatively, this can be understood because the breakdown threshold of metal surfaces are known to lie well below those of dielectrics.<sup>4</sup> Thus, the irradiation of unprotected, dielectric laser-fusion targets may lead to significant light leakage into the interior of the target. It is not clear at this time if this light can change the bulk of the target shell in any appreciable manner prior to plasma formation on the surface, nor do we know if such a change may depend on the detailed target composition (e.g., layered targets, including cryogenic targets). If the target shell and any possible cryogenic layer could be perturbed by the leakage of low-intensity laser light, the subsequent hydrodynamics of the collapsing shell could be changed and would be expected to lead to reduced target performance.

### Single-Beam Experiments

A number of experiments have been carried out recently at LLE to investigate the effects of light leakage through the surface of the target prior to plasma formation. These experiments were carried out on the glass development laser (GDL) under target and irradiation configurations indicated in Fig. 35.17. The primary diagnostic in these experiments consisted of microscopic inspection of the bulk plastic target material after laser irradiation.

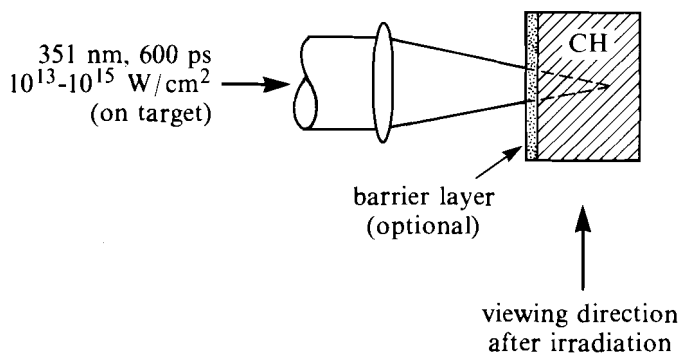
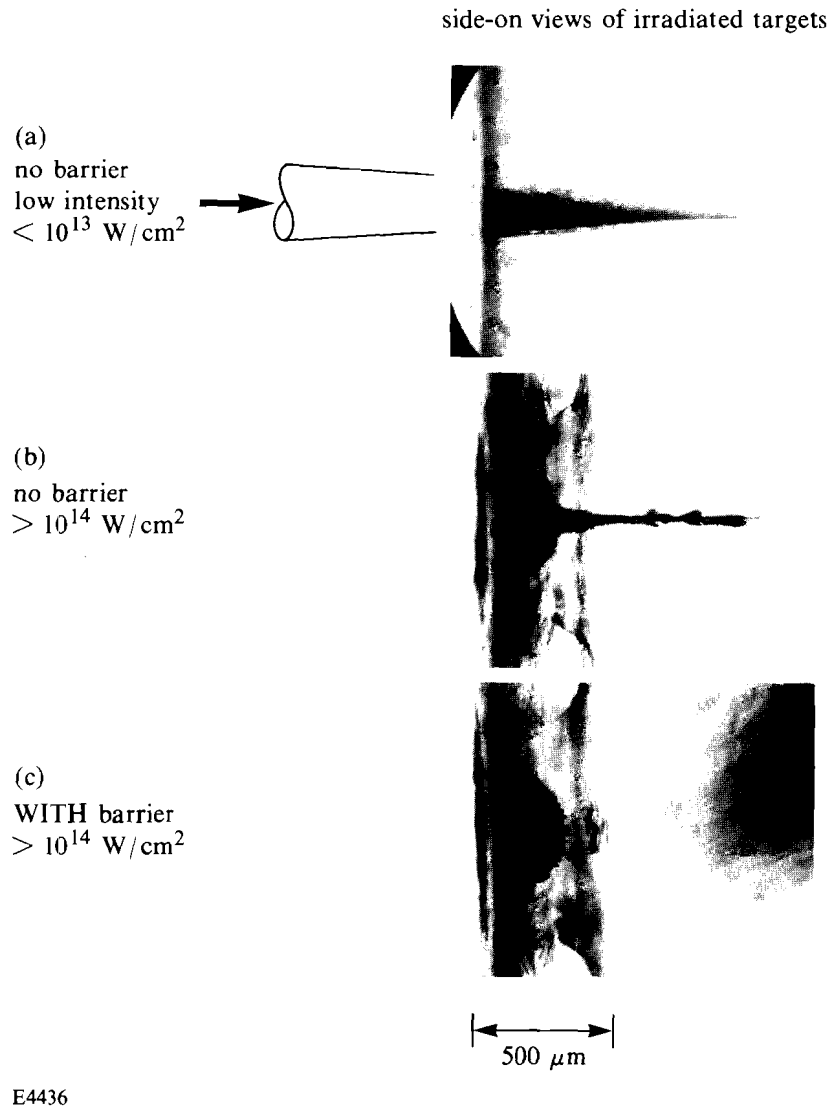


Fig. 35.17  
Target and irradiation configurations of single-beam (GDL) experiments with barrier-layer targets.

E4437

The main results of the single-beam experiments are illustrated in Fig. 35.18, which shows microscope photographs taken of solid plastic (Plexiglas) targets after irradiation by a 351-nm, 600-ps laser beam at various intensities between  $10^{13}$  and  $10^{15}$  W/cm<sup>2</sup>. The effects of conventional self-focusing or filamentation at low irradiation intensities are easily discernible in Fig. 35.18(a), while the effects of early light leakage at high irradiation intensities are shown in Fig. 35.18(b) and 35.18(c) for targets without and with thin barrier layers, respectively. The barrier layers consisted of up to 500 Å of Au or up to 1000 Å of Al evaporated on the surface of the target. In Fig. 35.18(b), one also observes what appears to be whole-beam self-focusing, as opposed to the small-scale filamentation visible in Fig. 35.18(a), the latter reflects the conical shape of the converging laser beam (nominal focus was approximately 700 μm inside the target), while the former collapses on axis well before the nominal focus. It is apparent from these photographs that the addition of a thin metal surface layer reduces the light leakage into the interior of the target [Fig. 35.18(c)], although nothing can be deduced from these images regarding any effects taking place within the first 200 μm of the target surface.

While these single-beam experiments illustrate—as have earlier experiments using 1-μm light—that there is some light leakage into the interior of the target prior to surface plasma formation, even for 351-nm irradiation, we have not yet succeeded in determining the amount of light leakage nor its effect on targets that are only several microns thick. However, we may speculate that in the presence of



E4436

Fig. 35.18  
Microscope photographs of Plexiglas targets after irradiation by 600-ps, 351-nm laser pulses of varying intensity: (a)  $\leq 10^{13}$  W/cm<sup>2</sup> without barrier layer; (b)  $\geq 10^{14}$  W/cm<sup>2</sup> without barrier layer; and (c)  $\geq 10^{14}$  W/cm<sup>2</sup> with 500-Å Al barrier layer. The nominal focus was  $\sim 700$  μm inside the target. Small-scale filamentation is apparent in (a), while whole-beam self-focusing appears to have occurred in (b). The hemispherical crater created by the surface plasma ablation and the subsequent shock waves are apparent in (b) and (c).

impurities or target imperfections, such leakage may cause breakdown inside the target<sup>5</sup> with concomitant problems expected for high-performance, laser-fusion compression experiments. Follow-up experiments on this subject are in progress.

#### 24-Beam OMEGA Experiments

The OMEGA experiments on barrier-layer targets fall into two categories—one using special multilayer signature targets to determine x-ray burn-through times, and the other using high-performance, DT-filled glass microballoons with and without plastic overcoating.

The burn-through times for various layer thicknesses of CH are typically determined from multilayer targets such as are shown in Fig.

35.19, which also illustrates the multilayer targets used in these experiments. The temporal emission from a metal signature layer buried below a CH layer is related to the laser pulse using an x-ray streak camera with an absolute laser fiducial imprinted on the record. Typical streak records of an Au signature layer buried below a  $6\text{-}\mu\text{m}$  CH layer show an abnormally early rise of the Au signal in the absence of any barrier layer, while a  $500\text{-}\text{\AA}$  Al barrier layer significantly delays the onset of the Au emission. In fact, when these data are compared with one-dimensional hydrodynamic simulations,<sup>3</sup> one finds that the temporal behavior of the signals from the signature layer obtained with the barrier layer is in fairly good agreement with the simulations, while those without the barrier layer cannot be explained on the basis of these or similar two-dimensional simulations. Our present experiments do not, however, permit us to determine the processes involved in causing the enhanced apparent burn-through rates in the absence of barrier layers. We suspect that the origin of these effects is the same as that causing the self-focusing channels in the single-beam, solid-plastic-target experiments. It may also be argued that with the absence of signature layers (buried metal or other high-Z layers), no damage may occur to targets of dimensions ( $<20\ \mu\text{m}$ ) typical for present-day laser-fusion experiments. However, Bloembergen<sup>5</sup> has shown that bulk and surface imperfections or impurities, or simple dielectric interfaces with microstructure, may significantly lower the breakdown threshold. Thus, it would be natural to assume that all or most present-day laser-fusion targets may suffer decreased interface breakdown thresholds, which could either destroy

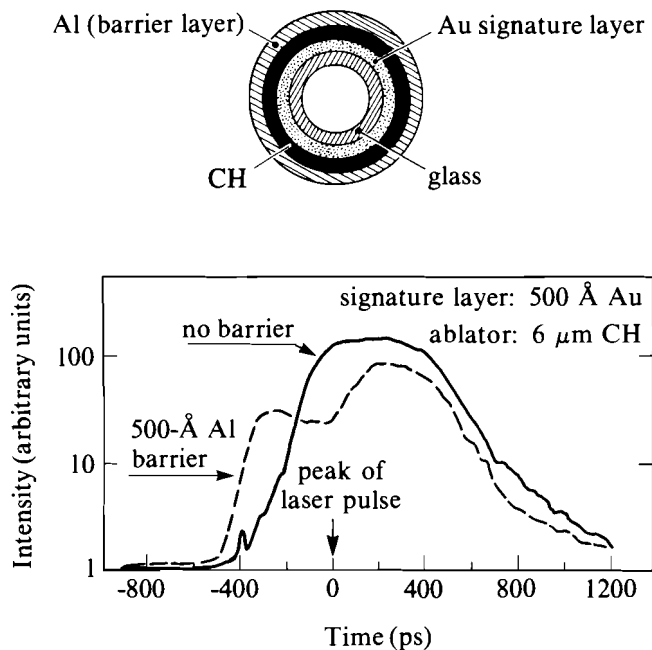


Fig. 35.19  
Multilayer target configurations and temporal evolution of x-ray signals from signature layers buried below  $6\ \mu\text{m}$  of CH under spherical irradiation conditions. Note the delayed onset of the Au emission with targets overcoated with  $500\ \text{\AA}$  of Al.

E4422

the integrity of the target shell or contaminate the fuel with shell debris. (Note that the inside surface of typical laser-fusion targets are generally less well characterized than are the outside surfaces.)

At present, our knowledge is insufficient to determine all the implications of early light leakage in direct-drive laser-fusion experiments. For the near term, it appears that thin metal barrier layers (surface coatings of a few hundred angstroms) are sufficient to prevent the most damaging problems of light leakage during the low-intensity rising part of the incident laser pulse.

OMEGA experiments using glass microballoons (GMB's) with or without CH ablator layers of up to 10  $\mu\text{m}$  have shown for some time that plastic-overcoated targets perform much worse (i.e., have much lower than expected neutron yield) than bare GMB's when compared with one- or two-dimensional hydrocode simulations. Overcoating these targets with  $<500 \text{ \AA}$  of Al has generally raised the neutron yields (such thin layers have negligible influence on the hydrodynamics or the predicted neutron yields). However, they have typically failed to raise the fuel  $\langle\rho R\rangle$  correspondingly. At this point, we are not able to explain the details of these observations, but we suspect that problems relating to irradiation uniformity mask part of the present data. Further investigations of these subjects are in progress.

#### ACKNOWLEDGMENT

This work was supported by the U. S. Department of Energy Office of Inertial Fusion under agreement No. DE-FC08-85DP40200 and by the Laser Fusion Feasibility Project at the Laboratory for Laser Energetics, which has the following sponsors: Empire State Electric Energy Research Corporation, New York State Energy Research and Development Authority, Ontario Hydro, and the University of Rochester. Such support does not imply endorsement of the content by any of the above parties.

#### REFERENCES

1. J. Delettrez, D. Bradley, P. Jaanimagi, M. C. Richardson, and S. Skupsky, *Bull. Am. Phys. Soc.* **32**, 1740 (1987).
2. J. E. Balmer, T. P. Donaldson, W. Seka, and J. A. Zimmermann, *Opt. Commun.* **24**, 109 (1978).
3. W. Seka, T. J. Kessler, S. Skupsky, F. J. Marshall, P. A. Jaanimagi, M. C. Richardson, J. M. Soures, C. P. Verdon, and R. Bahr, 18th European Conference on Laser Interaction with Matter (ECLIM), Prague, CSR, 4-8 May 1987, p. 52.
4. See, for example, Roger Wood, *Laser Damage in Optical Materials* (Adam Hilger, Bristol & Boston, 1986).
5. N. Bloembergen, *IEEE J. Quantum. Electron.* **J-QE 10**, 375 (1974).



## Section 2

# ADVANCED TECHNOLOGY DEVELOPMENTS

### 2.A Laser Damage in $\pi$ -Electron Systems

Organic, conjugated  $\pi$ -electron molecular and polymeric materials offer great promise for high-power laser applications. Their advantage over conventional materials lies in the flexibility that organic synthesis offers for their design. By the same approach that leads to the design of other organic compounds, especially pharmaceutical ones, organic materials with specific linear or nonlinear optical properties can now be defined, designed, and calculated in terms of response. The most important properties in this regard are absorption at certain wavelengths, nonlinear susceptibilities, fast response times, and high-power laser-damage thresholds.

The OMEGA laser is among the first to employ organic optical devices in significant numbers.<sup>1</sup> The majority of these devices are liquid-crystal-based circular polarizers developed and manufactured in house. Other devices use the linear birefringence of monomeric liquid-crystal molecules and usually comprise an eutectic mixture of several types of such molecules. In preparing any devices for  $5 \text{ J cm}^{-2}/1\text{-ns}$  applications, the question arises whether an improved laser-damage threshold can be engineered in an acceptable tradeoff with other parameters by changing the eutectic's composition. After elimination of compounds because of unsuitable linear absorption properties, the choice is between highly conjugated and more saturated compounds.

There are predictions that the nonlinear optical susceptibilities of organic systems are affected by the degree of conjugation. For  $\chi^{(2)}$ ,

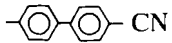
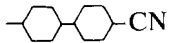
ample experimental evidence<sup>2</sup> supports this contention. For  $\chi^{(3)}$ , less data exist. Because  $\chi^{(3)}$  affects self-focusing, and because in the absence of extrinsic impurities self-focusing is a dominant mechanism for laser damage in many transparent materials, we tested the extent to which the damage threshold in some organic materials is affected by the degree of conjugation.

### Experiments

Three model compounds were chosen for this test: two monomers and one polymer. We report first on the nematic monomers and then on the cholesteric polymer. One monomeric,  $\pi$ -electron-rich compound was 4-octyl-cyanobiphenyl, which is a liquid crystal with a nematic mesophase at room temperature. Its saturated counterpart, 4-octyl-cyanobicyclohexyl, was also tested. As shown in Fig. 35.20, the two compounds differ structurally only in their aromatic and saturated cores. The bicyclohexyl compound is commercially available under the trade name ZLI-S-1185 and has a nematic phase starting at 62°C.<sup>3</sup> Laser interaction tests were conducted at 1053 nm (fundamental of Nd:phosphate glass laser), where neither material exhibits any resonance. This is substantiated by the two absorption scans in Fig. 35.21, obtained from 1-cm-path-length cells at elevated temperatures keeping the compounds in their respective isotropic phases. The 1053-nm absorption coefficient for the biphenyl compound was  $3.6 \times 10^{-2} \text{ cm}^{-1}$ . For the saturated compound, the residual absorption was three times larger. Absorption measurements were done in the isotropic phase to minimize the scattering contribution to the extinction.

Fig. 35.20

A comparison between a highly conjugated and an equivalent highly saturated liquid-crystal system shows that the laser polarizability of the saturated system rises the near-IR laser damage threshold.

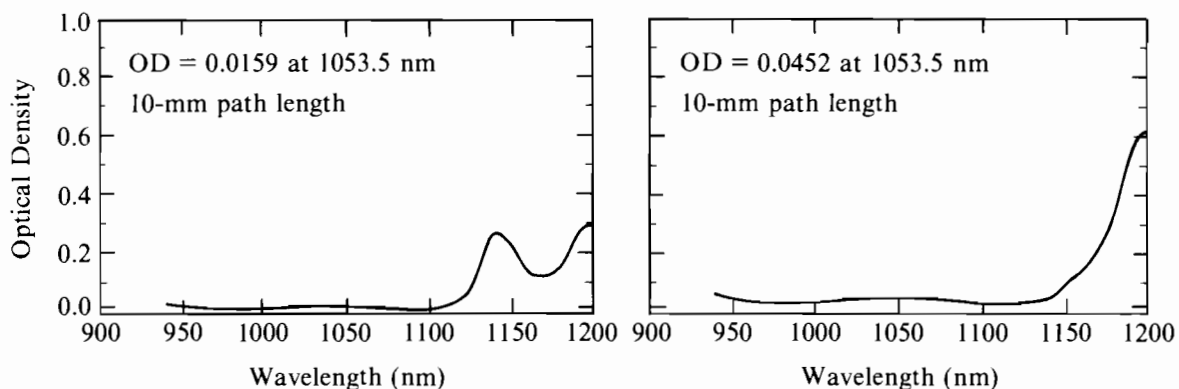
Compound	K-15	ZLI-1185
Structure	$\text{CH}_3-(\text{CH}_2)_4$  CN	$\text{CH}_3-(\text{CH}_2)_4$  CN
Mesophase	nematic (22°C)	nematic (62°C)
1-on-1 (J/cm <sup>2</sup> )	9.6±2.4	>16.6*
N-on-1 (J/cm <sup>2</sup> )	5.4±1.3	14.6±0.5

800-ps pulse length, 100- $\mu\text{m}$  path length, 5-mm spot size, linear polarization

\*for given spot size, transport optics damage at 20 J/cm<sup>2</sup>

G2247

Tests with linearly polarized incident pulses of 800-ps length were conducted identically for both monomeric materials. Unaligned cells of 100- $\mu\text{m}$  path length were prepared from 30-60-90 borosilicate prisms and uncoated, fused-quartz cuvette covers and were sealed by high-temperature epoxy. (A clarification for this choice of sample geometry



G2322

Fig. 35.21

The damage-test experiments were carried out at a wavelength where neither of the liquid-crystal samples exhibit any resonances. The residual linear absorption of 1053 nm of the saturated compound is higher than that of the conjugated, and yet its damage threshold is also higher.

is forthcoming in print.<sup>4</sup>) Cells were filled, by capillary action, with materials in their isotropic-fluid phase. Because this involves elevated temperatures, cells were not equipped with the organic alignment layers that are often used in aligning liquid crystals in either homeotropic or homogeneous configurations. It is also important to note that to date we have not found an alignment material that by itself shows a damage threshold in excess of the ones reported here for liquid crystals. What is frequently measured in tests of liquid-crystal/alignment-layer systems is therefore not the damage threshold of the liquid crystal but that of the alignment layer. A project currently under way aims at sorting out the alignment materials with the highest damage threshold.

Irradiation by high-peak-power laser pulses occurred at normal incidence. The beam was weakly focused to a spot size of about 3 mm. Laser-induced sample changes that in liquid crystals usually appear as small bubbles can be observed with a long-working-distance microscope. The detectability of bubbles was limited by the lifetime of bubbles that redissolve into the liquid matrix. One-on-1 and *N*-on-1 irradiation modes were chosen. In *N*-on-1 testing, each separate sample site was irradiated by series of ten pulses each (8% pulse-to-pulse energy stability) of slowly increasing fluence levels. In that mode, occurrence of damage was checked after each shot. After the appearance of a bubble, irradiation was terminated even if that bubble happened to redissolve. In *N*-on-1 testing, the interval between pulses was 5 s. A record of peak fluence and its location within the beam was obtained for each shot.

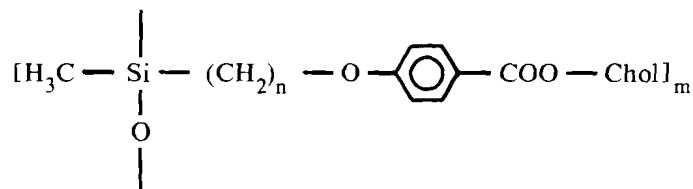
### Results

Results for the monomeric materials are listed in Fig. 35.20. For both the aromatic and saturated compounds, the *N*-on-1 threshold is lower than the 1-on-1 threshold. This is in general agreement with many other monomeric liquid-crystal compounds tested earlier. However, in both 1-on-1 and *N*-on-1 results, a significant difference is

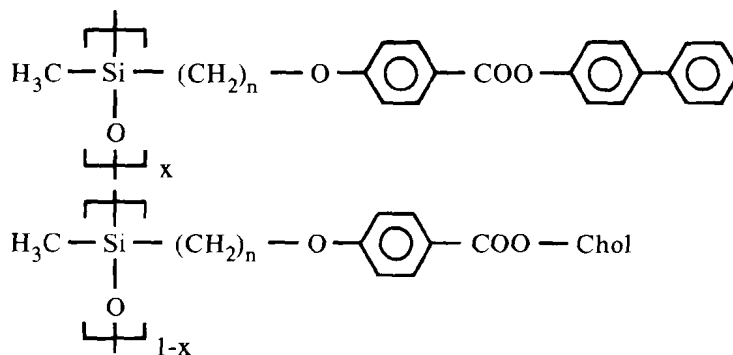
apparent between the  $p$ -electron-rich and the fully saturated nematic. In fact, the beam transport optics for this experiment suffered damage of its own before any site of the saturated compound showed single-shot bubble formation. The corresponding fluence level is twice that of the single-shot threshold average for the aromatic compound. The  $N$ -on-1 threshold comparison shows an improvement over the aromatic compound by nearly a factor of 3.

To eliminate from consideration that impurities may cause these threshold differences, we analyzed sample stock by gas chromatography. At the one-part-in- $10^5$  sensitivity level, no extraneous signals were observed from either compound. The only unusual feature was an isomer signature from the bicyclohexyl material. Within the stated sensitivity limit, impurities must be ruled out as a damage-dominating mechanism. Similarly, the opposing trends of damage thresholds and linear-absorption coefficients between the two nematics make linear absorption an unlikely damage mechanism.

The polymeric material was tested in a different approach. Here, the  $\pi$ -electron-rich phenyl functional group, one of several of the polymer's functional groups, was simply removed in the preparation of the control-sample polymer. The liquid-crystal polymer comprised a polysiloxane backbone with lateral, mesogenic side groups. The structure of the repeat unit is shown below:



Chol stands here for cholesterol;  $m$  is usually 4 or 5. The cholesterol functional group with its alkyl tail introduces chirality into the polymer, offering interesting optical properties. Among them is the coupling between the molecular helix and the proper-handed, circularly polarized light of a wavelength  $\lambda$  that matches the pitch of the helix. By varying the pitch of the chiral structure, tuned optical devices can be prepared.<sup>5</sup> One method for varying the pitch of a chiral nematic polymer is to prepare a variable-weight copolymer of the design



in which the density  $x$  of interleaved copolymer pendants determines the degree of pitch dilation along the backbone direction. By virtue of the  $\pi$ -electron distribution in the copolymer, changing this density means increasing or decreasing the nonlinear optical susceptibility of the total system in accordance with copolymer content. Testing the damage threshold of chiral copolymer samples tuned to different (nonresonant with regard to the 1053-nm incident wavelength) wavelengths provides further corroboration for the postulated link between  $\chi^{(3)}$  and the degree of conjugation.

Damage-test samples of the copolymer were prepared by dissolving the material in toluene and spraying about 100- $\mu\text{m}$ -thick films onto carefully cleaned, 30-60-90 borosilicate glass prism surfaces. Film thicknesses were uniform to better than 10% across individual samples but varied by up to 20% from sample to sample. The three copolymers reported here had cholesteric weight percents of 14%, 21%, and 35%, corresponding to tuned-response peak wavelengths of 1170 nm, 760 nm, and 450 nm, respectively. In 1-on-1 tests conducted in the same way as for monomeric materials, an important trend emerged: the copolymer with the highest cholesterol content—i.e., that with the lowest volume density of conjugation—showed the highest damage threshold; the one with the lowest cholesterol content and therefore the highest volume density of conjugation showed the lowest threshold. This trend is evident in Table 35.III.

Table 35.III  
Damage Thresholds of Cholesteric Copolymers

Weight % Cholesteric	Peak Wavelength (nm)	Film Thickness ( $\mu\text{m}$ )	1-on-1 Threshold ( $\text{J}/\text{cm}^2$ )	N-on-1 Threshold ( $\text{J}/\text{cm}^2$ )
14	1170	108	$0.8 \pm 0.1$	<0.8
21	760	104	$2.4 \pm 0.3$	0.8
35	450	83	$5.1 \pm 1.2$	<0.8
smectic-C	not applicable	105	$5.8 \pm 0.3$	$13.8 \pm 3.0$

G2414

Catalysts used in the synthesis of these polymers were thought to affect these thresholds through platinum trace residues. Platinum inclusions in laser glass have been widely acknowledged as prime damage-inducing impurities.<sup>6</sup> However, tests with especially purified copolymer samples yielded only marginally higher damage thresholds than those listed in Table 35.III. We surmise that the role of impurities in the IR laser damage of these materials is as insignificant as in the monomeric compounds. The damage morphology in polymers differed from monomers in that no bubbles were observed. Damage was monitored at the same spatial resolution as in the case of bubbles, except that here permanent structural modifications in the form of microscopic pits were recorded.

Finally, a cholesteric polymer was prepared that totally lacked the copolymer pendants used in the previous examples for wavelength tuning. It also lacked the phenol group in the cholesteric pendant. Except for one conjugated bond on the cholesterol itself, this system was entirely  $\pi$ -electron free. These reductions affected not only the laser damage threshold but other physical properties as well. The polymer glass transition temperature, affecting the material's processability, was raised and its mesogenic phase behavior changed. The chiral nematic room-temperature phase changed to smectic-C. Again, special efforts were made to keep this compound platinum-free. The platinum content was verified to be  $< 1$  ppm. When films of this material were prepared from a toluene solution in the same manner as for previous polymer samples, laser-damage thresholds could be measured. The 1054-nm, 1-on-1 threshold was  $5.8 \pm 0.3$  J/cm<sup>2</sup>, a 10% improvement over the best copolymer mentioned earlier. A more dramatic improvement was observed for the *N*-on-1 threshold. Whereas the  $\pi$ -electron-rich copolymers exhibited a common, precipitous threshold drop with large scatter in data to about 0.8 J/cm<sup>2</sup> when tested in the *N*-on-1 mode, the smectic-C sample showed a significant rise in threshold to  $13.8 \pm 3.0$  J/cm<sup>2</sup>. To date, we have no compelling explanation for these diverging trends. These measured thresholds compare well with the ones obtained for traditional, dielectric thin films.<sup>7</sup>

### Summary

To summarize, we conclude that, once impurities have been removed as a major cause of damage in organic optical materials, the volume density of conjugation in a compound becomes the dominant laser-damage factor. Because of this link, a reformulation of liquid-crystal polarizer compositions is under way that will enhance the damage resistance of liquid-crystal optical elements used in the OMEGA laser. The guiding principle here is to substitute, wherever possible, highly saturated compounds for conjugated ones. One trade-off in this case is a drop in birefringence associated with the loss in conjugation, a trade-off easy to accommodate. The same principle will also help make other liquid-crystal devices high-power compatible, such as soft apertures,<sup>8</sup> cholesteric laser end mirrors,<sup>9</sup> or active devices, such as shutters and modulators.<sup>10</sup>

### ACKNOWLEDGMENT

Dr. F. Kreuzer of Consortium für Elektrochemische Industrie, Munich, West Germany, kindly provided the polymeric sample materials and their analytical characterization. He also offered valuable advice.

This work was supported by the U.S. Department of Energy Office of Inertial Fusion under agreement No. DE-FC08-85DP40200 and by the Laser Fusion Feasibility Project at the Laboratory for Laser Energetics, which has the following sponsors: Empire State Electric Energy Research Corporation, New York State Energy Research and Development Authority, Ontario Hydro, and the University of Rochester. Such support does not imply endorsement of the content by any of the above parties.

### REFERENCES

1. S. D. Jacobs, K. A. Cerqua, K. L. Marshall, A. Schmid, M. J. Guardalben, and K. J. Skerrett, SPIE Proceedings Vol. 895 (to be published).

2. J. F. Nicoud, *Mol. Cryst. Liq. Cryst.* **156**, 257 (1988); H. E. Katz *et al.*, *J. Amer. Chem. Soc.* **109**, 6561 (1987).
3. Materials supplied by EM Chemicals, 5 Skyline Drive, Hawthorne, NY 10532.
4. S. D. Jacobs, K. A. Cerqua, K. L. Marshall, A. Schmid, M. J. Guardalben, and K. J. Skerrett, "Liquid-Crystal Laser Optics: Design, Fabrication, and Performance," *J. Opt. Soc. Amer. B* (to be published).
5. I. P. Il'Chisin, E. A. Tirhonov, V. G. Tishechenro, and M. T. Shpak, *JETP Lett.* **32**, 24 (1980).
6. D. Milam, C. W. Hatcher, and J. H. Campbell, in Seventh Annual Symposium on Optical Materials for High Power Lasers, *Nat. Bur. Stand. (U.S.), Spec. Publ.* (to be published).
7. T. Walker, A. Guenther, and P. Nielsen, *IEEE J. Quantum Electron.* **QE-17**, 2041 (1981).
8. LLE Review **24**, 188 (1985).
9. Yu. V. Denisov, V. A. Kizel, V. A. Orlov, and N. F. Perevozchirov, *Sov. J. Quantum Electron.* **10**, 1447 (1980).
10. R. A. Soref, *Opt. Lett.* **4**, 155 (1979).

## Section 3

# NATIONAL LASER USERS FACILITY NEWS

National Laser Users Facility (NLUF) activity during the third quarter of FY88 supported the projects of **J. G. Jernigan** of the University of California at Berkeley (UCB), **H. Griem** of the University of Maryland, **U. Feldman** of the Naval Research Laboratory, and **J. Apruzese** of the Naval Research Laboratory. This support centered on planning for future experiments and diagnostic development of these groups.

J. G. Jernigan is continuing the development of a two-dimensional readout for active x-ray imaging. This group has taken delivery of a  $256 \times 256$  amplifier array that is bonded to a pin diode array. This device was manufactured by the Hughes Research Laboratory and is an integral part of the next step in the active imaging work being done by the Space Sciences Laboratory at UCB. During Dr. Jernigan's visit to LLE plans were finalized for the installation of this readout array onto the back of an x-ray pinhole camera, which is to be fielded onto the OMEGA target chamber. **F. Marshall** of LLE is collaborating with the UCB group and will assist in the measurements on the OMEGA system.

OMEGA will be changed to line focus during July 1988 for experiments to be done by H. Griem, U. Feldman, and J. Apruzese. These individuals visited LLE in preparation for their upcoming experiments. The details of how the line focus targets would be aligned and what diagnostics would be needed were discussed. All of the line focus experiments will be done during this time to facilitate the operation of OMEGA. These experiments are to measure thermal transport, atomic spectroscopy, and electron interactions in linear plasmas.



## Section 4

# LASER SYSTEM REPORT

### 4.A GDL Facility Report

The GDL system was in service during the entire quarter as a target interaction facility. Campaigns undertaken with the GDL system included an extensive investigation of laser propagation through aerosol media in conjunction with the U.S. Army CRDEC; electro-optic focussing experiments; time-resolved uniformity measurements of the GDL beam; and continued x-ray laser studies. For the laser-propagation study, a new target chamber, vacuum system, and diagnostic package were installed in the Beta target room.

A summary of GDL operations this quarter follows:

Beamline Test, Calibration, Tuning, and Laser Alignment Shots	156
Target Shots	
LLE-CRDEC	186
Electro-Optic Focussing	142
Uniformity Measurement	77
X-Ray Laser	102
Other	<u>37</u>
TOTAL	700

## 4.B OMEGA Facility Report

The OMEGA laser and target system has been out of operation as a target illuminator for this reporting period. Shutdown has provided the time necessary to complete major maintenance activities on OMEGA. In addition to maintenance, upgrades to our alignment system and laser diagnostics have been implemented, improving our capabilities in IR and UV alignment and transport optics measurement.

Since OMEGA has 30 m of path and eight optical components between the frequency-conversion crystals and the target chamber center, a cw UV alignment system has been introduced that provides means to accurately assess the losses of each component in the transport path. Ultraviolet alignment and diagnosis can now be accomplished using a cw, 351-nm beam coaligned with any beamline at the output of the crystal structure. In addition to providing the capability of observing the UV light retroreflected from the target in each beam, the UV alignment table (UVAT) incorporates a precision ratiometer to allow accurate (to 1%) measurement of transport optics losses to the center of the chamber. Improvements have been implemented into the existing IR alignment table. Liquid-crystal polarizers have been installed, thereby improving the polarization of the YLF beam and allowing more energy to be properly coupled into individual beamlines. A CID camera has been installed on the table, allowing improved viewing of the retroreflected beam from the target chamber for ease of targeting.

During this quarter fused silica plates with a novel thin-film coating have been fabricated and will be used to reject remaining IR energy in the beams after frequency conversion. The plates, dubbed "red dumps," are mounted on kinematic bases for easy installation and removal. As we return to operation, we will observe the effect of shielding the beamlines from potentially damaging IR energy backscattered from targets. Another possible benefit of the red dumps is the reduction of IR energy incident on experimental chamber surfaces.

Plasma calorimetry has been refurbished during the shutdown. An entirely new electronics package provides direct measurement of energy incident on both the ring and disc of the differential calorimeter. By processing the data from each calorimeter element independently, problems that have troubled plasma calorimetry during the last campaigns may be eliminated. Hardware that accompanies the electronics, consisting of a new calorimeter mount, aperture, shutter, and an in-situ calibration system, has been designed and prototyped.

An all new computer-controlled vacuum system has been implemented on the OMEGA target chamber. The new vacuum controller gives the experimental and operational personnel a global picture of vacuum status in the experimental chamber and on individual diagnostics.

In the area of OMEGA uniformity, substantial progress has been made since last quarter. Off-line testing of electro-optic beam-deflection schemes has been accomplished. Project goals are speckle smoothing of the phase-converted OMEGA beams on target, yielding improved irradiation uniformity. The beam analysis table (BAT), a laser diagnostic system used for phase measurement of the pulsed UV beams, is nearing activation in OMEGA. The BAT is installed on a track system allowing rapid installation into any beamline. During the reactivation and characterization period of the shutdown, several alternative uniformity improvements were pursued. Along with complete calibration of the laser-energy-measurement systems, a new technique for temporal analysis of the laser pulse was developed. A system was implemented that has the capability of monitoring the pulse width of several beams simultaneously using fibers to transport the beams to a single streak-camera photocathode. A system for analyzing all 24 beams on a streak camera is undergoing design and procurement for deployment in September.

As the quarter was dedicated to improving laser performance and beam quality, there have been a number of driverline and laser test shots. Target shots have been limited to laser characterization, plasma calorimeter testing, vacuum system testing, and target systems reactivation.

A summary of OMEGA operations for this quarter follows:

Target Shots	10
Driver Line Shot and Tests	28
Laser Test and Alignment Shots	<u>109</u>
TOTAL	147

**ACKNOWLEDGMENT**

This work was supported by the U. S. Department of Energy Office of Inertial Fusion under agreement No. DE-FC08-85DP40200 and by the Laser Fusion Feasibility Project at the Laboratory for Laser Energetics, which has the following sponsors: Empire State Electric Energy Research Corporation, New York State Energy Research and Development Authority, Ontario Hydro, and the University of Rochester. Such support does not imply endorsement of the content by any of the above parties.

# PUBLICATIONS AND CONFERENCE PRESENTATIONS

## Publications

D. R. Dykaar, R. Sobolewski, J. M. Chwalek, J. F. Whitaker, T. Y. Hsiang, G. A. Mourou, D. K. Lathrop, S. E. Russek, and R. A. Buhrman, "High-Frequency Characterization of Thin-Film Y-Ba-Cu Oxide Superconducting Transmission Lines," *Appl. Phys. Lett.* **52**, 1444-1446 (1988).

K. A. Cerqua, J. E. Hayden, and W. C. LaCourse, "Stress Measurements in Sol-Gel Films," *J. Non-Cryst. Solids* **100**, 471-478 (1988).

B. Yaakobi, D. Shvarts, T. Boehly, P. Audebert, R. Epstein, B. Boswell, M. C. Richardson, and J. M. Soures, "X-Ray Laser Studies at LLE," *Short and Ultrashort Wavelength Lasers* (SPIE, Bellingham, WA, 1988), Vol. 875, pp. 9-19.

K. A. Cerqua, M. J. Shoup III, D. L. Smith, S. D. Jacobs, and J. H. Kelly, "Strengthened Phosphate Glass in a High Rep Rate Active-Mirror Geometry," *Appl. Opt.* **27**, 2567-2572 (1988).

P. Bado, M. Pessot, J. Squier, G. A. Mourou, and D. J. Harter, "Regenerative Amplification in Alexandrite of Pulses from Specialized Oscillators," *IEEE J. Quantum Electron.* **24**, 1167-1171 (1988).

J. F. Seely, U. Feldman, C. M. Brown, M. C. Richardson, D. D. Dietrich, and W. E. Behring, "Transitions in Na-Like and Mg-Like Ions of Ln, Sb, I, and Cs," *J. Opt. Soc. Am. B* **5**, 185 (1988).

K. L. Marshall and S. D. Jacobs, "Near-Infrared Dichroism of a

Mesogenic Transition Metal Complex and Its Solubility in Nematic Hosts," *Mol. Cryst. Liq. Cryst.* **159**, 197 (1988).

R. L. McCrory and J. M. Soures, "Fusion Progress Report: A Milestone Achieved," *The Scientist* **2**, 17-18 (1988).

## Forthcoming Publications

G. Mourou, "Picosecond Electro-Optic Sampling," to be published in the *Proceedings of the High Speed Electronics Conference*, Stockholm, Sweden, August 1986.

R. L. McCrory and J. M. Soures, "Inertially Confined Fusion," to be published in *Applications of Laser Plasmas*, Chapter 7.

P. C. Cheng, H. Kim, D. M. Shinozaki, K. H. Tan, and M. D. Wittman, "X-Ray Microscopy - Its Application to Biological Sciences," to be published in the *Proceedings of the X-Ray Microscopy Meeting '87*, Stony Brook, NY, September 1987 (Springer-Verlag).

W. Watson, "Vacuum-Assisted Contaminated Particulate Removal," to be published in the *Journal of Vacuum Science and Technology*.

R. L. McCrory, J. M. Soures, C. P. Verdon, F. J. Marshall, S. A. Letzring, S. Skupsky, T. J. Kessler, R. L. Kremens, J. P. Knauer, H. Kim, J. Delettrez, R. L. Keck, and D. K. Bradley, "Laser-Driven Implosion of Thermonuclear Fuel to 20 to 40 g cm<sup>-3</sup>," to be published in *Nature*.

R. L. McCrory, J. M. Soures, C. Verdon, M. Richardson, P. Audebert, D. Bradley, J. Delettrez, L. Goldman, R. Hutchison, S. Jacobs, P. Jaanimagi, R. Keck, H. Kim, T. Kessler, J. Knauer, R. Kremens, S. Letzring, F. Marshall, P. McKenty, W. Seka, S. Skupsky, and B. Yaakobi, "High-Density Laser-Fusion Experiments at the Laboratory for Laser Energetics," to be published in the *Proceedings of the 8th International Workshop on Laser Interaction and Related Plasma Phenomena*.

C. A. Amsden, S. E. Gilman, S. D. Jacobs, and J. S. Torok, "Measurement of the Thermal Conductivity of Dielectric Thin Solid Films with a Thermal Comparator," to be published in *The Optical Interference Coatings 1988 Technical Digest*.

W. E. Behring, J. H. Underwood, C. M. Brown, U. Feldman, J. F. Seely, F. J. Marshall, and M. C. Richardson, "Grazing Incidence Technique to Obtain Spatially Resolved Spectra from Laser-Heated Plasmas," to be published in *Applied Optics*.

R. Q. Gram, C. K. Immesoete, H. Kim, and L. Forsley, "Bounce-Coated Ablation Layers on Fusion Targets," to be published in the *Journal of Vacuum Science and Technology*.

P. Maine and G. Mourou, "Amplification of 1 ns Pulses in Nd:Glass Followed by Compression to 1 ps," to be published in *Optics Letters*.

P. C. Cheng, S. P. Newberry, H. Kim, and M. D. Wittman, "X-Ray Contact Microradiography and Shadow Projection X-Ray Microscopy," to be published in the *European Journal of Cell Biology*.

W. R. Donaldson, "Radial Line Structure Experiments," to be published in the *Proceedings of the 4th Workshop: Pulse Power Techniques for Future Accelerators*, Erice, Sicily, 3-10 March 1988.

S. E. Goldsmith, J. C. Moreno, H. R. Griem, L. Cohen, and M. C. Richardson, "Relative Ion Expansion Velocity in Laser-Produced Plasmas," to be published in the *Journal of Applied Physics*.

K. L. Marshall, A. W. Schmid, D. J. Smith, A. A. Bevin, M. J. Guardalben, and S. D. Jacobs, "Performance of Protective Polymeric Coatings for Nonlinear Optical Materials," to be published in the *Journal of Applied Physics*.

S. D. Jacobs, K. A. Cerqua, K. L. Marshall, A. Schmid, M. J. Guardalben, and K. J. Skerrett, "Liquid Crystal Laser Optics: Design, Fabrication, and Performance," to be published in the *Journal of the Optical Society of America B*.

J. C. Lee, J. H. Kelly, D. L. Smith, and S. D. Jacobs, "Gain Squaring in a Cr:Nd:GSGG Active Mirror Amplifier Using a Cholesteric Liquid Crystal Mirror," to be published in the *IEEE Journal of Quantum Electronics*.

M. C. Richardson, D. K. Bradley, P. A. Jaanimagi, J. Delettrez, R. Epstein, C. F. Hooper, R. C. Mancini, and D. Kilcrease, "X-Ray Diagnosis of High-Density Compression of Ar-Filled Polymer Shell Targets," to be published in the *Review of Scientific Instruments*.

A. Simon and R. W. Short, "Alternative Analysis of CO<sub>2</sub>-Laser-Produced Plasma Waves," to be published in *Physics of Fluids*.

J. F. Whitaker, G. A. Mourou, T. C. L. G. Sollner, and W. D. Goodhue, "Switching-Time Measurements of a Resonant Tunneling Diode," to be published in *Applied Physical Letters*.

## Conference Presentations

The following presentations were made at the 4th Topical Meeting on Optical Interference Coatings, Tucson, AZ, 12-15 April 1988:

C. J. Hayden and E. Spiller, "Large Area Coatings with Uniform Thickness Fabricated in a Small Vacuum Chamber."

C. A. Amsden, S. E. Gilman, S. D. Jacobs, and J. S. Torok, "Measurement of the Thermal Conductivity of Dielectric Thin Solid Films with a Thermal Comparator."

---

The following presentations were made at the Conference on Superconductivity and Applications, Buffalo, NY, 18-21 April 1988:

G. Mourou, D. Dykaar, J. Chwalek, and J. Whitaker, "Superconducting Interconnects."

D. R. Dykaar, J. M. Chwalek, J. F. Whitaker, R. Sobolewski, T. Y. Hsiang, and G. A. Mourou, "High-Frequency Characterization of Thin-Film Y-Ba-Cu Oxide Superconducting Transmission Lines: Experiment and Simulation."

---

The following presentations were made at CLEO '88, Anaheim, CA, 25–29 April 1988:

S. Williamson, "Millimeter Depth Resolution, Streak-Camera-Based Lidar."

P. Maine and G. Mourou, "Amplification of 1-ns Pulses in Nd:Glass Followed by Compression to 1 ps."

W. Donaldson and L. E. Kingsley, "Electro-Optic Imaging of Semiconductor Contact Fields."

J. F. Whitaker, G. A. Mourou, T. C. L. G. Sollner, and W. D. Goodhue, "Switching Time Measurements of a Resonant Tunneling Diode."

J. M. Chwalek, D. R. Dykaar, R. Sobolewski, J. F. Whitaker, T. Y. Hsiang, G. Mourou, D. K. Lathrop, S. E. Russek, and R. A. Buhrman, "Propagation Characteristics of Picosecond Electrical Transients on  $\text{YBa}_2\text{Cu}_3\text{O}_{7-y}$  Transmission Lines."

M. Pessot, J. Squier, G. Mourou, P. Bado, and D. J. Harter, "Amplification of Femtosecond Pulses in an Alexandrite Regenerative Amplifier."

J. H. Kelly, D. L. Smith, J. C. Lee, S. D. Jacobs, M. J. Shoup III, and D. J. Smith, "An Improved Active Mirror Geometry Cr:Nd:GSGG Amplifier."

T. Kessler, W. Castle, N. Sampat, S. Skupsky, D. Smith, and S. Swales, "Phase Conversion for Fusion Lasers" (invited talk).

J. Nees, ">100-GHz Velocity-Matched Traveling Wave Modulator."

J. S. Coe, P. Bado, and P. Maine, "Gain Narrowing in a Nd:YLF cw-Pumped Regenerative Amplifier."

---

D. J. Smith, "Advances in Optical Coating Technology: New Applications and Improvements in Process and Measurement," presented at the 24th Annual Symposium of the New Mexico Chapter of the American Vacuum Society, Albuquerque, NM, 19–21 April 1988.

H. Kim, "Applications of High-Power Lasers," presented at the '88 Korea Congress on Science and Technology – Spring Workshop, Seoul, Korea, 10–12 May 1988.

W. R. Donaldson, P. Basseras, C. Bamber, and A. Melissinos, "Ultrafast High Power Switching: Techniques and Applications," presented at the Optically and Electron-Beam Controlled Semiconductor Switches Workshop, Norfolk, VA, 23–24 May 1988.

J. M. Chwalek, J. F. Whitaker, and D. R. Dykaar, "High-Frequency Characterization of Thin-Film Y-Ba-Cu Oxide Superconducting Transmission Lines: Experiment and Simulation," presented at the 1988 IEEE MTT-S International Microwave Symposium, New York, NY, 23–27 May 1988.

A. Simon and R. W. Short, "Nonlinear Aspects of Enhanced Plasma Wave Model of Raman Scattering," presented at the Joint US/USSR

Workshop on the Nonlinear Physics of Dense Plasma, Santa Fe, NM, 23–28 May 1988.

G. Mourou, D. Dykaar, J. Chwalek, J. Whitaker, and K. Meyer, "Ultrafast Optics for Superconducting and Semiconducting Electronics," presented at the 13th Nordic Semiconductor Meeting, Stockholm, Sweden, 5–8 June 1988.

M. L. Tsai, S. H. Chen, K. L. Marshall, and S. D. Jacobs, "Thermotropic and Optical Properties of Chiral Nematic Polymers," presented at the 10th Symposium on Thermophysical Properties, Gaithersburg, MD, 20–23 June 1988.

---

The following presentations were made at the 6th Target Fabrication Specialists' Meeting, Los Alamos, NM, 20–24 June 1988:

H. Kim and M. D. Wittman, "X-Ray Microscopy of Inertial Fusion Targets Using a Laser-Produced Plasma as an X-Ray Source."

H. Kim, R. Q. Gram, and J. M. Soares, "Ablation Layer Coating on Inertial Fusion Targets at University of Rochester's Laboratory for Laser Energetics."

S. Letzring, H. Kim, F. J. Marshall, R. L. McCrory, J. M. Soares, C. P. Verdon, R. Gram, C. Hestdalen, R. Keck, R. Kremens, G. Pien, O. Lopez-Raffo, F. Rister, and M. Wittman, "Development, Implementation, and Operational Characteristics of an Improved Cryogenic-Target-Positioning System."

---

The following presentations were made at the Upstate New York Chapter of the American Vacuum Society, Rochester, NY, 22–24 June 1988:

M. Jolly, C. A. Amsden, S. D. Jacobs, and S. E. Gilman, "Thermal Conductivity Measurements of Dielectric Thin-Film Optical Coatings."

C. J. Hayden and E. Spiller, "Large Area Coatings with Uniform Thickness Fabricated in a Small Vacuum Chamber."

R. S. Craxton, "Laser-Fusion Research: Progress and Prospects" (invited talk).

---

The following presentations were made at the 18th Annual Anomalous Absorption Conference, l'Esterel, Quebec, 26 June–14 July 1988:

S. H. Batha, D. D. Meyerhofer, W. Seka, A. Simon, L. M. Goldman, C. B. Darrow, R. P. Drake, and D. S. Montgomery, "Observations of Raman Up-Scatter in a Long-Scale-Length Plasma."

D. K. Bradley, J. Delettrez, R. Epstein, C. Hestdalen, and P. A. Jaanimagi, "Recent Experimental Measurements of Laser Burnthrough on Plastic-Coated Microballoons."

R. S. Craxton, "Two-Dimensional Hydrodynamics and Refraction in X-Ray Laser Experiments."

J. Delettrez, D. K. Bradley, R. Epstein, and P. A. Jaanimagi, "Theoretical Analysis of Burn-Through Experiments in Targets with Barrier Layers."



- E. M. Epperlein, "Non-Local Thermal Smoothing Effects in Laser-Produced Plasmas."
- G. G. Luther, S. H. Batha, and C. J. McKinstrie, "Efficiency Enhancement of the Conjugate Signal for a Collinear Four-Wave Mixing Process."
- F. J. Marshall, S. A. Letzring, C. P. Verdon, J. P. Knauer, D. K. Bradley, T. Kessler, J. Delettrez, H. Kim, J. M. Soures, and R. L. McCrory, "Cryogenic-Laser-Fusion-Target Implosion Studies Performed with the OMEGA UV Laser System."
- R. W. Short, "The Effect of Self-Focusing on Hot Spots in Multiple-Beam Illumination Geometries."
- A. Simon and R. W. Short, "Energy and Nonlinearity Considerations for the Enhanced Plasma Wave Model of Raman Scattering."
- R. Epstein, J. Delettrez, D. K. Bradley, P. A. Jaanimagi, and P. D. Goldstone, "Non-LTE Simulation of Time-Dependent Features of X-Ray Spectra from High-Z Targets."
- D. D. Meyerhofer, R. S. Craxton, and J. Delettrez, "Calculations of Collisional Energy Deposition in Short-Scale-Length Plasmas."
- S. V. Coggeshall, P. D. Goldstone, W. C. Mead, D. K. Bradley, P. A. Jaanimagi, J. Knauer, F. J. Marshall, G. Pien, and M. C. Richardson, "Simulations and Analysis of a Recent Spherical X-Ray Conversion Efficiency Experiment."
- P. D. Goldstone, J. A. Cobble, W. C. Mead, S. V. Coggeshall, D. K. Bradley, P. A. Jaanimagi, J. Knauer, F. J. Marshall, G. Pien, M. C. Richardson, J. F. Seely, and U. Feldman, "Observations of Symmetry-, Density-, and Z-Dependence of X-Ray Conversion."
- 
- D. R. Dykaar, J. M. Chwalek, J. F. Whitaker, R. Sobolewski, T. Y. Hsiang, and G. A. Mourou, "High Frequency Characterization of Thin-Film Y-Ba-Cu Oxide Superconducting Transmission Lines: Experiment and Simulation," was presented at the NATO Advanced Study Institute on Superconducting Electronics, Ciocco, Italy, 26 June-8 July 1988.

#### ACKNOWLEDGMENT

The work described in this volume includes current research at the Laboratory for Laser Energetics, which is supported by Empire State Electric Energy Research Corporation, New York State Energy Research and Development Authority, Ontario Hydro, the University of Rochester, and the U.S. Department of Energy Office of Inertial Fusion under agreement No. DE-FC08-85DP40200.

